Journal of Nuclear Medicine, published on August 12, 2021 as doi:10.2967/jnumed.121.262270

Title: Blind Image Restoration Enhances Digital Autoradiographic Imaging of Radiopharmaceutical Tissue Distribution

Authors: Peng Lu[1,2,3], Nadia Benabdallah[2,3], Wen Jiang[3,4], Brian W. Simons[5], Hanwen Zhang[2,3], Robert F. Hobbs[6], David Ulmert[7,8], Brian C. Baumann[9], Russell K. Pachynski[10], Abhinav K. Jha[1,2] & Daniel L.J. Thorek[1,2,3,11]

Affiliations:

[1]Department of Biomedical Engineering, Washington University in St. Louis
[2]Department of Radiology, Mallinckrodt Institute of Radiology, Washington University School of Medicine
[3]Program in Quantitative Molecular Therapeutics, Washington University School of Medicine
[4]Department of Biomedical Engineering, Johns Hopkins University
[5]Center for Comparative Medicine, Baylor College of Medicine
[6]Radiation Oncology and Molecular Radiation Sciences, Johns Hopkins University School of Medicine
[7]Department of Molecular and Medical Pharmacology, University of California, Los Angeles
[8]Ahmanson Translational Imaging Division, David Geffen School of Medicine, University of California, Los Angeles
[9]Department of Radiation Oncology, Washington University School of Medicine
[10]Division of Oncology, Washington University School of Medicine
[11]Oncologic Imaging Program, Siteman Cancer Center, Washington University School of Medicine

Corresponding Author:

Daniel LJ Thorek
Department of Radiology, Washington University in St. Louis,
510 S. Kingshighway Blvd. St. Louis, Missouri, 63110
314-747-5624 | thorekd@wustl.edu

First Author:

Peng Lu
Department of Radiology, Washington University in St. Louis,
510 S. Kingshighway Blvd. St. Louis, Missouri, 63110
314-747-5624 | penglu@wustl.edu

Running Title: Blind Restore Digital Autoradiogram

ABSTRACT

Digital autoradiography (DAR) is a powerful tool to quantitatively determine the distribution of a radiopharmaceutical within a tissue section and is widely used in drug discovery and development. However, the low image resolution and significant background noise can result in poor correlation, even errors, between radiotracer distribution, anatomical structure, and molecular expression profiles. Differing from conventional optical systems, the point spread function (PSF) in DAR is determined by properties of radioisotope decay, phosphor and digitizer. Calibration of an experimental PSF a priori is difficult, prone to error, and impractical. We have developed a content-adaptive restoration algorithm to address these problems.

Methods: We model the DAR imaging process using a mixed Poisson-Gaussian model, and blindly restore the image by a Penalized Maximum-Likelihood Expectation-Maximization algorithm (PGPEM). PG-PEM implements a patch-based estimation algorithm with "Density-Based Spatial Clustering of Applications with Noise" to estimate noise parameters, and utilizes L2 and Hessian Frobenius (HF) norms as regularization functions to improve performance.

Results: First, PG-PEM outperformed other restoration algorithms at the denoising task ($p<0.01$). Next, we implemented PG-PEM on pre-clinical DAR images (^{18}F-FDG treated mice tumor and heart, ^{18}F-NaF treated mice femur) and clinical DAR images (bone biopsy sections from $^{223}RaCl_2$ treated castrate resistant prostate cancer patients). DAR images restored by PG-PEM of all samples achieved significantly higher effective resolution, contrast to noise ratio (CNR), and a lower standard deviation of background (STDB) ($p<0.0001$). Additionally, by comparing the registration results between the clinical DAR images and the segmented bone masks from the corresponding histological images, the radiopharmaceutical distribution was significantly improved ($p<0.0001$).

Conclusions: PG-PEM is able to increase resolution and contrast while robustly accounting for DAR noise, and demonstrates the capacity to be widely implemented to improve pre- and clinical DAR imaging of radiopharmaceutical distribution.

Keywords: Digital autoradiography; Blind image restoration; Poisson-Gaussian noise model; Positron; Alpha particle emission

INTRODUCTION

Autoradiography is a powerful, high resolution and quantitative molecular imaging technique used to study the tissue distribution of radioisotopes in biologic systems and for analytic assays (*1–4*). Originally, radioactivity distributions were acquired using photographic emulsions which are high resolution, but require time consuming, fickle, and variable processes. Currently, phosphor imaging plate-based digital autoradiography (DAR) has supplanted film due to its linear activity response, non-destructive approach, no chemical-processing requirement, large dynamic range and considerable sensitivity (*2,4,5*).

Generally, DAR is performed by placing tissue samples containing radioactivity apposed to the phosphor screen which absorbs and stores the energy of the radioactive emissions, creating a "latent image" of activity distribution (Fig. 1A). Except for very low energy beta emitters (tritium), the phosphor layer and the specimens are typically separated by low-attenuation film to prevent contamination of the screen itself, and exposure lasts hours to days. The phosphor plate is raster scanned with a small focal-spot red laser, and the photostimulated light is collected by a photomultiplier tube to form a digital image (Fig. 1B). The intensity of emitted light is proportional to the amount of radioactivity in the tissue sample.

Suboptimal image quality in DAR limits assessment of radioligand evaluation. Unlike optical microscopy systems, DAR does not utilize an aperture or collimator, and the solid angle subtended at the samples by the imaging plate is almost 2π. Therefore, the point spread function (PSF) results from isotropic emission and is dependent on a combination of energy dispersion in the phosphor, plate properties (lattice and grain size) and readout laser, and physical properties also make the PSF isotope-dependent. Additionally, replicating relevant features of the signal for DAR acquisitions in a phantom is difficult. In aggregate, it is thus not practical to calibrate the PSF beforehand.

Apart from blurring effects caused by PSF, background signal is always present in imaging process caused by environmental radiation. DAR noise can be attributed to multiple sources: Poisson noise exists in the photon counting imaging system; Gaussian noise comes from the imaging reader readout process, phosphor

sheet inhomogeneities and grain (*6*). Few approaches have been tested to overcome noise and blur-related artifacts: a regularized iteration method after noise filtration (*7*) and the modeling of noise features (*8*). The results from these investigations are not ideal and have not been widely adopted, in part, because several have used an emulsion film-based system (the predecessor to phosphor storage plate technology) and noise amplification effects. Common to these approaches are pre-calibration of PSF by non-ideal resolution phantom.

In order to model the noise in DAR systems of many isotopes, a blind estimation approach for restoration is preferred. Recently, a mixed noise model has been employed to denoise digital images, which can improve the quality of images contaminated by Poisson and Gaussian noise sources (*9–12*). A key step in such a model is estimation of noise parameters. For single image restoration, patch-based (*9*), segmentation-based (*11*) or Fourier-based (*12*) methods have been developed; and several blind and non-blind image restoration techniques for biomedical images have been advanced (*13–19*). For the specific task of blind restoration, the regularizations for PSF and specimen are considered in some of these methods, providing a path forwards for blind DAR estimation.

Here, a blind image restoration algorithm based on a mixed Poisson-Gaussian noise model and penalized maximum likelihood expectation maximization (MLEM) algorithm, PG-PEM, is presented. We first describe this model in the context of the DAR imaging process along with a patch-based noise parameter estimation method. We incorporate a penalized MLEM algorithm to jointly estimate the restored specimen image and corresponding PSF. L2 and Hessian Frebonius (HF) norms are implemented for PSF and specimen signal separately, to improve quality of the restored image. PG-PEM improves resolution, contrast, and suppresses noise more effectively than contemporary restoration approaches, using both pre- and clinical applied diagnostic and therapeutic radiopharmaceuticals.

MATERIALS AND METHODS

Mice Tumor, Heart and Femur Preparation

Experiments were performed in accordance with approved protocols (Institutional Animal Care and Use Committee Protocol #2019006). Male C57Bl/6 mice (6-10 weeks) from Jackson Laboratory (Bar Harbor, Maine) were administered approximately 200 μCi (7.4 MBq) of either ^{18}F-FDG or ^{18}F-NaF and sacrificed at 1 h. Tissues were embedded in optimal cutting temperature media, frozen on dry ice, and sectioned at 8 μm by cryostat (CM188, Leica). For all radiographic exposures, MS phosphor plates were exposed at -20 °C and read using a Cyclone Plus (Perkin Elmer) with unit of "digital light unit" (DLU). We then used ImageJ (*20*) to crop regions of interest.

Human Bone Biopsy Preparation

Bone biopsies were obtained from seven metastatic castrate resistant prostate cancer (mCRPC) patients under fluoroscopic guidance following a bone scan, 24 h after injection of $^{223}RaCl_2$. The institutional review board approved this study (Human Research Protection Office Protocol #201411135) and all subjects provided written informed consent. The biopsy was fixed in 4% paraformaldehyde for 24 h and transferred to 30% sucrose for 24h, frozen, cut and imaged (above).

Staining and Imaging

Sections were stained with hematoxylin and eosin (H&E) and scanned at 10× (Nikon Eclipse Ti2 for the mice tumor, heart and femur slides; Zeiss Axio Scan Z1 for human bone biopsy slides).

Overview of Image Formation Model and Restoration Algorithm

According to the DAR imaging process, its physical model can be expressed as Eq. (1),

$$R_p = \alpha Q_p + N_p, Q_p \sim \mathcal{P}\left[(X * h)_p + b_p\right], N_p \sim \mathcal{N}(0, \sigma_G^2), \quad (1)$$

where p is the pixel index, R the raw image, α the scaling factor corresponding to the gain of the imaging system, X the "clean" radioactive signal, h the PSF, b the mean of background, $\mathcal{P}[x]$ the Poisson noise with mean x, and $\mathcal{N}(0, \sigma_G^2)$ the Gaussian-distributed readout noise with mean of 0 and standard deviation σ_G. Here, we assume b_p is invariant because of the homogeneous radiation around the tissue.

To estimate X, a careful modelling of Gaussian noise $\mathcal{N}(0, \sigma_G^2)$ and Poisson noise $\alpha\mathcal{P}[b]$ from background b is necessary. We implement a noise model to jointly estimate parameters of the two components. This is based on the fact that Poisson distribution can be feasibly approximated by a Gaussian distribution when $b > 3$ (*21*) (Supplementary Fig. 1). Notably, this condition is always satisfied for DAR imaging and therefore, the two independent noise features are summed into a new single Gaussian-distributed noise (Supplementary Note 1.1). Consequently, the raw image can be re-organized into Poisson-distributed signal: $\alpha\mathcal{P}[X_p * h]$ and Gaussian-distributed noise: $\mathcal{N}(\mu_N, \sigma_N^2)$ with mean of αb and variance of $\alpha^2 b + \sigma_G^2$. Obviously, $\mathcal{N}(\mu_N, \sigma_N^2)$ describes the statistical characterization of the background of DAR images.

Non-tissue areas in DAR should only have background and noise, and be highly similar to each other. From this assumption, we propose a patch-based estimation algorithm based on "density based spatial clustering of applications with noise" (*22*) (Fig. 1C(1), Supplementary Note 1.2 (*23*), Supplementary Algorithm 1 and Supplementary Fig. 2) to robustly segment background and estimate μ_N and σ_N.

The PG-PEM algorithm uses these noise parameters and the raw image to blindly estimate X based on a penalized MLEM algorithm (Fig. 1C(2), Supplementary Notes 1.3 and 1.4 (*24,25*)). The E step aims to eliminate the Gaussian-distributed noise $\mathcal{N}(\mu_N, \sigma_N^2)$ by calculating the expectation of $X * h$ while the M step deconvolutes the blurry image corrupted by Poisson-distributed data by jointly estimating h and X. In practice, the blind deconvolution problem is highly ill-posed. Through the iteration process, h tends to converge towards a delta function because of high frequency noise in the specimen image. To avoid the trivial solution and considering the smooth characteristics of h, it is regularized by L2 norm. L2 norm is linearly correlated to the power of h. Therefore, the smaller L2 norm, the smaller the power of h is and thus, the smoother h is. During the same

process, the noise of the estimated X may be amplified. Total variation (TV) is a popular approach (*16,19*) to suppress such noise by restraining the summation of the derivative of an image, according to the empirical summary that signals are usually successive while noise arises randomly. However, TV oversharpens boundaries between different regions, generating a "staircase" effect. To avoid this artifact, we implemented HF norm regularization to enable smoother transitions between different regions and to suppress noise simultaneously (*15,17,18*). Compared to TV regularization, HF is a second-order derivative norm and forces the second-order derivative to be sparse. The continuity between different pixels agrees more with the characteristics of biological autoradiogram data. The regularization strengths for h and X are controlled by their regularization parameters λ_h and λ_X, respectively.

For our novel PG-PEM, initial estimates for h and X are needed. The raw image R is set as the initial guess of X divided by α. h can be initialized based on the imaging model. Apart from even scattering, making h circularly symmetric, the finite focal point effect of the image reader and the modulation transfer function of the phosphor plate have minor effects on h. However, it is unnecessary to build a PSF model accounting for all effects in a blind restoration framework. Instead, h is initialized based on the inverse square law (*26*) when only considering the scattering (Supplementary Note 1.5, Supplementary Fig. 3). Finally, the scaling factor α must be calibrated. Methods previously presented for optical imaging (*11,18*) are insufficiently robust for DAR images because it is difficult to find enough homogeneous regions to calibrate α. Empirical calibration is impractical and generally infeasible because of the stochastic decay process and short half-lives in DAR. Fortunately, the mixed Poisson-Gaussian data can be approximated as a shifted-Poisson form (*18*) and further in the deconvolution of Poisson-distributed images, results are not affected by this scaling parameter. Thus, PG-PEM yields a calibration-free algorithm when α is set in a proper range (Supplementary Note 1.6). The detailed algorithmic framework and runtime analysis are summarized (Supplementary Note 1.7, Supplementary Algorithm 2 and Supplementary Table 1).

Quality Metrics

For experiments, the full-width half-maximum (FWHM), standard deviation of the background (STDB) and contrast to noise ratio (CNR) are set as the accuracy metrics due to the lack of ground truth. FWHM and STDB can evaluate the resolution and noise level separately, while CNR assessed overall performance.

For DAR it is difficult to measure FWHM using micro-beads. Alternatively, we use a recently published decorrelation-based method (*27*) (Supplementary Fig. 4). This method does not estimate the theoretical resolution of the imaging system, but the highest frequency with sufficiently high signal in relation to noise. We refer to the estimated FWHM as effective resolution.

For simulations, accuracy metrics include root mean squared error, signal power to noise power ratio (SNR) and structural similarity (SSIM) (*28*), with which the estimated images can be compared with the ground truth directly. These metrics along with CNR are defined in Supplementary Note 2.

Statistical Analysis

Quantitative data are presented as box-and-whisker plots (center line, median; limits, 75% and 25%; whiskers, maximum and minimum). We used paired two-side Student's t-test to compare data of Raw and PG-PEM restored DAR images, and the paired one-way analysis of variation to compare all other data (Prism 8; GraphPad Software Inc.). Statistical significance at $P<0.05$, 0.01, 0.001 and 0.0001 are denoted by *, **, *** and ****, respectively.

RESULTS

Assessment of Image Enhancement

We benchmarked performance of several restoration frameworks: Richardson-Lucy (RL) (*13*), RL with wavelet-based residue denoising (RD) (*29*), Shift-Poisson (SP) (*18*), PG-PEM with no regularization for X (NP) and PG-PEM with TV regularization (TV). For comparison, we have applied our novel background reduction and blind restoration to all approaches, and tuned h to be similar (Supplementary Notes 3.1–3.5). PG-PEM together with the five modified reference algorithms were implemented on both simulated (Supplementary Note 4.1) and experimental images. Regularization parameters are tuned (Supplementary Note 4.2, Supplementary Figs. 5–6) and comparisons on simulated data are analyzed (Supplementary Note 4.3, Supplementary Figs. 7–11).

DAR images (n=10) acquired from the mouse hindlimb following ^{18}F-NaF PET imaging were used as experimental data and to evaluate the performance of image restoration approaches. As is standard for short lived diagnostic radioisotopes and required tissue-processing, sectioning and exposure times, the SNR of the raw images are low, providing a model setting for comparison. Visual assessment and analyses (Figs. 2 and 3, Supplementary Fig. 12) show implementation of restoration algorithms improved resolution and suppressed noise to varying magnitudes. Log-scale images reveal NP, TV and PG-PEM have more homogeneous background than other methods, a result of splitting the image components into Poisson-distributed signal and Gaussian-distributed noise. The non-homogeneous background in RL, RD and SP correspond to noise and false positive signal generated in their restoration process.

Next we assessed the log-scale amplitude of the Fourier space. Because h is isotropic, the resolution of DAR images should be at least quasi-isotropic. Curiously, we observed that high frequencies tended along the horizontal direction and are highly non-isotropic, which correspond to the noise. By comparing the frequency maps of NP, TV and PG-PEM, the non-isotropic components of NP have the highest energy. TV produces a broader non-isotropic frequency portion than PGPEM and a “staircase” effect. These along with STDB and CNR

indicate that PG-PEM is the best denoiser. Meanwhile, RL, SP, NP, TV and PG-PEM share similar quasi-isotropic areas in the dotted black circles, while that of RD has the lowest energy. The resolution of RD is the lowest because wavelet-denoising processes remove fine details. With a MLEM restoration framework (and the same regularization strategy for PSF *h*), RL, SP, NP, TV and PG-PEM share similar resolutions. Notably, due to the lack of a regularization strategy for *X*, the resolution of NP may be slightly higher than those of the other methods, which can be neglected due to the impact of noise. The effective resolution improves at least 5-fold after restoration by PG-PEM ($P<0.0001$). These data along with the simulation results demonstrate that PG-PEM is the best performer for blind restoration of DAR images.

PG-PEM Improves DAR of Diagnostic Radiopharmaceuticals

To determine whether PG-PEM could improve the quality of DAR images in diagnostic radiopharmaceuticals we investigated distribution of the widely used metabolic tracer ^{18}F-FDG, and bone seeking ^{18}F-NaF, in tissue samples from mice tumor, heart and femur (n=10 per group). We used PG-PEM to restore these data, calculated STDB, CNR, and effective resolution for comparison to the raw images (Fig. 4). These results demonstrate the image quality improvement after restoration. Notably, non-glycolytic (prostate) tumor section which takes up little ^{18}F-FDG has extremely low SNR. Nevertheless, PG-PEM suppresses background noise and improves resolution of regions of uptake (Supplementary Fig. 13). RL and SP algorithms were chosen as references to restore the same DAR images from ^{18}F-FDG treated tumors (Supplementary Fig. 14). Compared with PG-PEM, the results of RL and SP, especially their background components, have more apparent noise. The corresponding STDB and CNR reveal that PG-PEM is superior to restore DAR images under extremely low SNR conditions, with a $P<0.0001$.

We next asked if higher SNR images, from ^{18}F-FDG in the heart and ^{18}F-NaF in the bone, could likewise be improved by PG-PEM. From the raw cardiac images, radioisotope signal is almost homogeneous. By contrast,

the PG-PEM restored data has higher resolution and improved contrast which may better reflect the spatial distribution of the tracer (Supplementary Figs. 13 and 15). We further compared the H&E, raw and restored DAR images of the murine femur (Fig. 5, Supplementary Fig. 16). After restoration the endosteal and periosteal surfaces are clearly visualized, and the proximal head of the femur is resolved. Because the positron range of ^{18}F is considerable, its DAR is blurred compared to lower energy beta emitters or high-linear energy transfer alphas, which hinders assessment of radiopharmaceuticals distribution. Our results indicate that PG-PEM can ameliorate this issue, underscoring pre-clinical utility.

Enhanced Targeted Alpha Particle Radiotherapy Evaluation by PGPEM

Targeted delivery of alpha particle emitting radionuclides is an emerging application for metastatic cancer treatment (*30,31*). Analyzing the dose distribution for alpha particle therapy near the cell-scale plays a key role in predicting the treatment response and assessing the toxicity of this targeted paradigm, especially as their path length is at the microscopic scale. Current small-scale dosimetry methods are predominately based upon idealized computational anatomical models (*32,33*). While useful, these provide limited real-world information in heterogeneous patient populations.

We investigate alpha particle emitter activity distributions from a dataset of 10 bone biopsy slides of mCRPC patients treated with $^{223}RaCl_2$ (Fig. 6, Supplementary Fig. 17). The raw DAR images suffer from blur and noise due to the imaging process, distorting the true radiotracer distribution. This can cause large errors in registration, and degrades treatment response assessment and toxicity analysis. ^{223}Ra will adsorb on the bone surface (*34*) and the high activity regions should be located here. Based on this knowledge, DAR and histopathology images can be registered, and restoration algorithms evaluated.

After registration (Supplementary Fig. 18), raw and restored DAR images were fused with an anatomical bone mask (Supplementary Fig. 19). PG-PEM can not only improve the resolution and remove noise in these DAR, but also results in more accurate correlation with underlying anatomy. Quantitatively, line profiles, STDB

and CNR improve, and the effective resolution increases by approximately 1.7 folds over raw data (Fig. 7). We then calculated the SSIM between the high activity regions of DAR images with their segmented bone masks, and evaluated a Fusion Index, defined as the ratio of total activity at bone surfaces (Supplementary Fig. 20). Note that the higher SSIM and Fusion Index are, the better correlation between the modalities. The evaluation results show PG-PEM is able to improve these two accuracy metrics significantly ($P<0.0001$). Consequently, PG-PEM can be of great use in personalized targeted alpha particle radiotherapy assessment.

DISCUSSION

Autoradiography is an important technique in drug development and evaluation of radiolabeled compounds for imaging and targeted therapy (*35*–*38*). In particular, there is considerable academic, pharmaceutical industry and clinical interest to assess targeted alpha and beta particle emitters for endotherapy. Unlike external beam radiation delivery, systemically administered radionuclides can irradiate all tissues in the body and. localized distribution is central to calculate absorbed doses and to predict both treatment response and off-target toxicities. Conventional image formation methods using DAR suffer from noise and other image artifacts. In this work, we have defined and implemented a novel PG-PEM algorithm to restore blurred and noisy DAR data.

PG-PEM is based upon the DAR imaging process and a mixed Poisson-Gaussian noise model. The noise parameters are estimated with a patch-based algorithm after a Poisson-Gaussian distribution conversion. A penalized MLEM approach is then used to jointly estimate the specimen image and its corresponding PSF, simultaneously. Specifically, we used L2 norm to regularize the PSF to ensure its smoothness and avoid the trivial solution; and HF norm to regularize the estimated specimen image to ensure its continuity and to suppress noise. Notably, this approach effectively eliminates the “staircase” effect caused by TV regularization. As a consequence, even low SNR images are robustly restored. To the best of our knowledge, this is the first attempt to combine MLEM with Hessian norm-based regularization.

After analyzing the scaling factor α, we prove it is free of pre-calibration in PG-PEM. Subsequently, the algorithm was quantitatively compared against alternative approaches across multiple datasets. Because of the blind restoration framework, PG-PEM is not a convex problem and we cannot guarantee it can converge to a global solution. Nevertheless, simulation and experimental results show that PG-PEM is the lead performer, providing improved correlation between signal and tissue features.

Interestingly, even though both SP and PG-PEM are based upon the mixed Poisson-Gaussian noise model, PG-PEM has lower noise and reduced background false positive signal. This difference comes from the iteration process: PG-PEM first filters Gaussian-distributed noise in the E step and then filters Poisson-distributed noise in the M step. In addition, we have also compared the PSFs estimated from different isotopes ($^{223}RaCl_2$ treated human bone biopsy and ^{18}F-NaF treated mouse hindlimb). Clearly, the kernel size of the PSF from the hindlimb is larger than that from the biopsy (Supplementary Fig. 21), consistent with the physics of alpha/positron travel, further validating the blind restoration approach.

Recently, convolutional neural networks have proved effective in biomedical image restoration (*39,40*). However, it may not be well suited for DAR restoration because of multiparametric factors influencing PSF, noise characteristics for each isotope and tissue, and the lack of clean label data.

CONCLUSION

We have developed the PG-PEM algorithm for improved DAR image quality. Predicated on a complete image formation model for DAR and implementation of a signal and background segmentation approach, this blind image restoration approach reduced background noise and image blur in simulated and primary image samples. For both high and low SNR datasets, of diagnostic and therapeutic radionuclides, there were significant improvements in DAR resolution, contrast and accuracy of localization. This method will be widely applicable to both pre-clinical and clinical sample autoradiograms to improve radiotracer and radiotherapy agent evaluation.

DISCLOSURES

This work was funded in part by the National Cancer Institute of National Institutes of Health R01CA229893 (D.L.J.T.), R01CA201035 (D.L.J.T.) and R01CA240711 (D.L.J.T.), the Society of Nuclear Medicine and Molecular Imaging Student Research Award (P.L.). Authors report no conflict of interest relevant to this article.

KEY POINTS:

QUESTION: Can developments in computational imaging tools be leveraged to improve diagnostic tracer and therapeutic radionuclide distribution assessment on the tissue scale?

PERTINENT FINDINGS: A combination of noise-reduction along with automated image restoration leads to significantly enhanced digital autoradiographs. Background noise can be efficiently reduced, improved contrast, and enhanced resolution. Particular benefits are found for low SNR images as demonstrated on clinical bone biopsies from men treated with alpha particle emitting Radium-223.

IMPLICATIONS FOR PATIENT CARE: Improved understanding of radioisotope distribution at the tissue scale is expected to benefit target engagement studies for drug development and to enable more accurate dose distribution.

REFERENCES

1. Solon EG. Autoradiography: high-resolution molecular imaging in pharmaceutical discovery and development. *Expert Opin Drug Discov.* 2007;2:503–514.

2. Johnström P, Bird JL, Davenport AP. Quantitative phosphor imaging autoradiography of radioligands for positron emission tomography. *Methods Mol Biol.* 2012;897:205–220.

3. Bäck T, Jacobsson L. The α-camera: a quantitative digital autoradiography technique using a charge-coupled device for *ex vivo* high-resolution bioimaging of α-particles. *J Nucl Med.* 2010;51:1616–1623.

4. Griem-Krey N, Klein AB, Herth M, Wellendorph P. Autoradiography as a simple and powerful method for visualization and characterization of pharmacological targets. *J Vis Exp.* 2019;145:e58879.

5. Sonoda M, Takano M, Miyahara J, Kato H. Computed radiography utilizing scanning laser stimulated luminescence. *Radiology.* 1983;148:833–838.

6. Boncelet C. Chapter 7-Image noise models. In: *The Essential Guide to Image Processing.* Boston, MA: Academic Press; 2009:159–160.

7. Goyette J, Lapin G, Kang M, Katsaggelos AK. Regularized iterative image restoration algorithms applied to autoradiography. In: *Annu Int Conf IEEE Eng Med Biol Soc.* IEEE; 1993;490–491.

8. Zhang M, Chen Q, Li XF, *et al.* Image deconvolution in digital autoradiography: a preliminary study. *Med Phys.* 2008;35:522–530.

9. Jezierska A, Pesquet JC, Talbot H, Chaux C. Iterative Poisson-Gaussian noise parametric estimation for blind image denoising. In: *Proc Int Conf Image Proc.* IEEE; 2014:2819–2823.

10. Chouzenoux E, Jezierska A, Pesquet JC, Talbot H. A convex approach for image restoration with exact Poisson-Gaussian likelihood. *SIAM J Imaging Sci.* 2015;8:2662–2682.

11. Foi A, Trimeche M, Katkovnik V, Egiazarian K. Practical Poissonian-Gaussian noise modeling and fitting for single-image raw-data. *IEEE Trans Image Process.* 2008;17:1737–1754.

12. Mandracchia B, Hua X, Guo C, Son J, Urner T, Jia S. Fast and accurate sCMOS noise correction for fluorescence microscopy. *Nat Commun.* 2020;11:94.

13. Fish D, Brinicombe A, Pike E, Walker J. Blind deconvolution by means of the Richardson-Lucy algorithm. *J Opt Soc Am A Opt Image Sci Vis.* 1995;12:58–65.

14. Kenig T, Kam Z, Feuer A. Blind image deconvolution using machine learning for three-dimensional microscopy. *IEEE Trans Pattern Anal Mach Intell.* 2010;32:2191–2204.

15. Lefkimmiatis S, Bourquard A, Unser M. Hessian-based norm regularization for image restoration with biomedical applications. *IEEE Trans Image Process.* 2011;21:983–995.

16. Keuper M, Schmidt T, Temerinac-Ott M, *et al.* Blind deconvolution of widefield fluorescence microscopic data by regularization of the optical transfer function (OTF). In: *Proc IEEE Comput Soc Conf Comput Vis Pattern Recognit.* IEEE; 2013:2179–2186.

17. Huang X, Fan J, Li L, *et al.* Fast, long-term, super-resolution imaging with Hessian structured illumination microscopy. *Nat Biotechnol.* 2018;36:451–459.

18. Ikoma H, Broxton M, Kudo T, Wetzstein G. A convex 3D deconvolution algorithm for low photon count fluorescence imaging. *Sci Rep.* 2018;8:11489.

19. Koho S, Tortarolo G, Castello M, Deguchi T, Diaspro A, Vicidomini G. Fourier ring correlation simplifies image restoration in fluorescence microscopy. *Nat Commun.* 2019;10:3103.

20. Schindelin J, Arganda-Carreras I, Frise E, *et al.* Fiji: an open-source platform for biological image analysis. *Nat Methods.* 2012;9:676–682.

21. Janesick JR. Photon transfer noise sources. In: *Photon transfer DN→ λ.* Bellingham, Wash: SPIE Press; 2007:21–25.

22. Ester M, Kriegel HP, Sander J, Xu X. A density-based algorithm for discovering clusters in large spatial databases with noise. In: *KDD.* AAAI; 1996:226–231.

23. Crain BR. Estimating the parameters of a truncated normal distribution. *Appl Math Comput.* 1979;5:149–156.

24. Brune C, Sawatzky A, Burger M. Bregman-EM-TV methods with application to optical nanoscopy. In: *SSVM.* Elsevier; 2009:235–246.

25. Resmerita E, Anderssen RS. Joint additive Kullback-Leibler residual minimization and regularization for linear inverse problems. *Math Models Methods Appl Sci.* 2007;30:1527–1544.

26. Brownson JR. Chapter 03-Laws of light. In: *Solar Energy Conversion Systems.* Boston: Academic Press; 2014: 41–66.

27. Descloux AC, Grussmayer KS, Radenovic A. Parameter-free image resolution estimation based on decorrelation analysis. *Nat Methods.* 2019;16:918–924.

28. Wang Z, Bovik AC, Sheikh HR, Simoncelli EP. Image quality assessment: from error visibility to structural similarity. *IEEE Trans Image Process.* 2004;13:600–612.

29. Boussion N, Le Rest CC, Hatt M, Visvikis D. Incorporation of wavelet-based denoising in iterative deconvolution for partial volume correction in whole-body PET imaging. *Eur J Nucl Med Mol Imaging.* 2009;36:1064–1075.

30. Baidoo KE, Yong K, Brechbiel MW. Molecular pathways: targeted α-particle radiation therapy. *Clin Cancer Res.* 2013;19:530–537.

31. Abou D, Benabdallah N, Jiang W, *et al.* Prostate cancer theranostics-an overview. *Frontiers in Oncology.* 2020;10:884.

32. Sgouros G, F Hobbs R, Song H. Modelling and dosimetry for alpha-particle therapy. *Curr Radiopharm.* 2011;4:261–265.

33. Hobbs RF, Song H, Watchman CJ, *et al.* A bone marrow toxicity model for ^{223}Ra alpha-emitter radiopharmaceutical therapy. *Phys Med Biol.* 2012;57:3207–3222.

34. Abou DS, Ulmert D, Doucet M, Hobbs RF, Riddle RC, Thorek DL. Whole-body and microenvironmental localization of radium-223 in naive and mouse models of prostate cancer metastasis. *J Natl Cancer Inst.* 2016;108:djv380.

35. Solon EG, Kraus L. Quantitative whole-body autoradiography in the pharmaceutical industry: Survey results on study design, methods, and regulatory compliance. *J Pharmacol Toxicol Methods.* 2001;46:73–81.

36. Solon EG. Use of radioactive compounds and autoradiography to determine drug tissue distribution. *Chem Res Toxicol.* 2012;25:543–555.

37. McDevitt MR, Thorek DL, Hashimoto T, *et al.* Feed-forward alpha particle radiotherapy ablates androgen receptor-addicted prostate cancer. *Nat Commun.* 2018;9:1629.

38. Yang AC, Stevens MY, Chen MB, *et al.* Physiological blood–brain transport is impaired with age by a shift in transcytosis. *Nature.* 2020;583:425–430.

39. Weigert M, Schmidt U, Boothe T, *et al.* Content-aware image restoration: pushing the limits of fluorescence microscopy. *Nat Methods.* 2018;15:1090–1097.

40. Guo M, Li Y, Su Y, *et al.* Rapid image deconvolution and multiview fusion for optical microscopy. *Nat Biotechnol.* 2020;38:1337–1346.

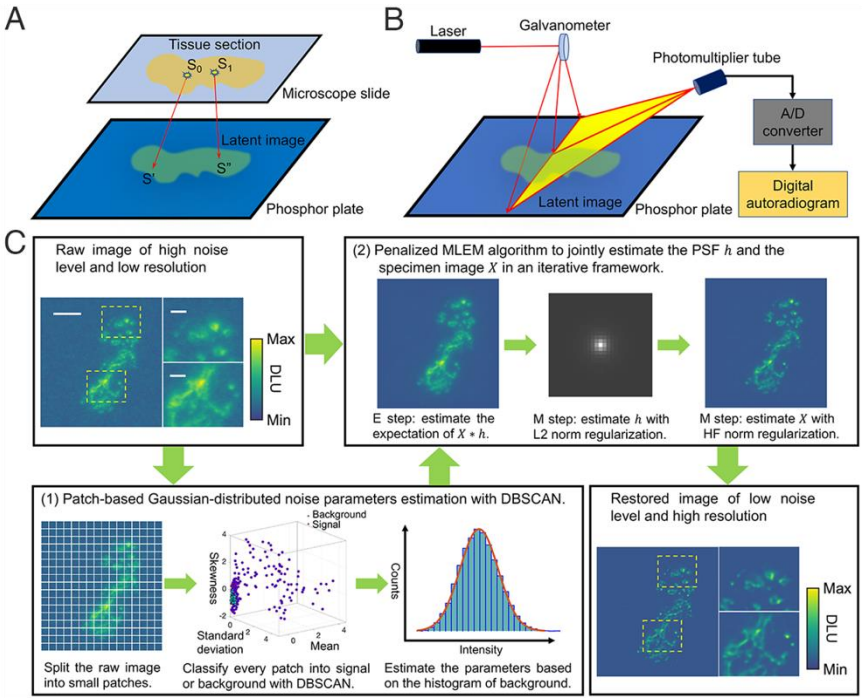

Fig. 1: DAR imaging process and PG-PEM algorithmic framework. (a) Latent image generation, in which S_0 and S_1 are two point sources, detected at *S'* and *S''*. (b) DAR image generation. (c) PG-PEM framework: (1): noise parameters estimation; (2): PSF and specimen image estimation. Scale bar: big figures: 2.3 mm, small figures: 0.54 mm.

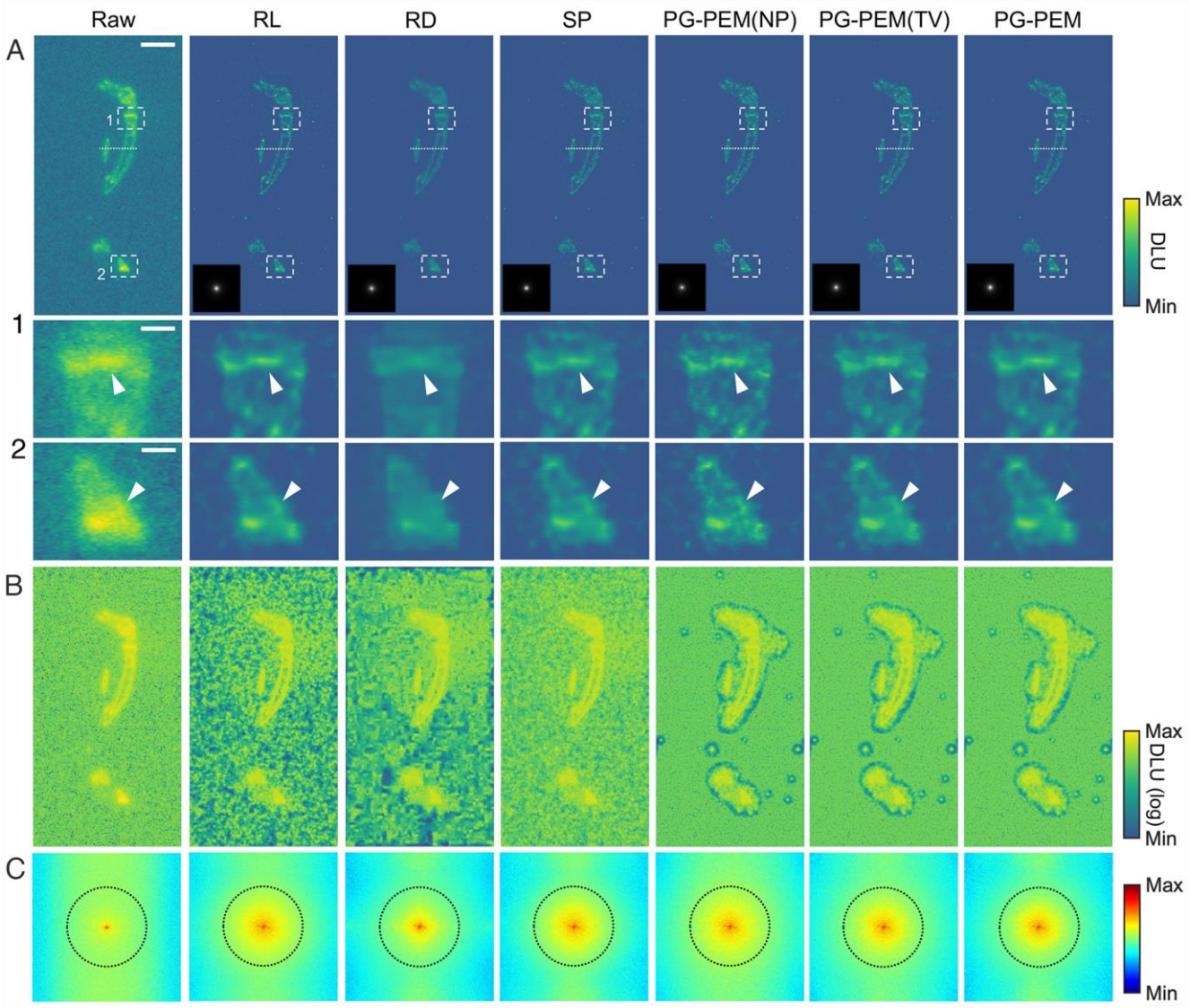

Fig. 2: Blind restoration improves DAR. (A) Raw DAR image from the mouse hindlimb following ^{18}F-NaF PET imaging and its restoration results using modified restoration algorithms. Estimated PSFs are inset in grey scale. (B) Log-scale transformed images from (A) for background appraisal. (C) Log-scale amplitude of the Fourier transform of raw and restored images from (A). Scale bar: (A): 4.95 mm, (A1) and (A2): 0.86 mm.

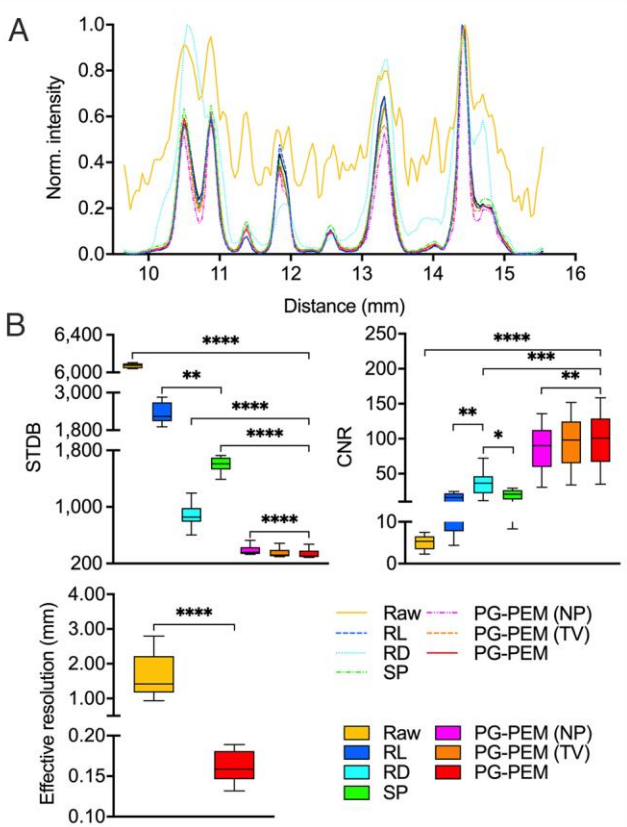

Fig. 3: Quantitative assessment of different blind restoration approaches. (A) Profiles of the dashed lines in Fig. 2(A). (B) STDB, CNR and effective resolution comparisons of the approaches.

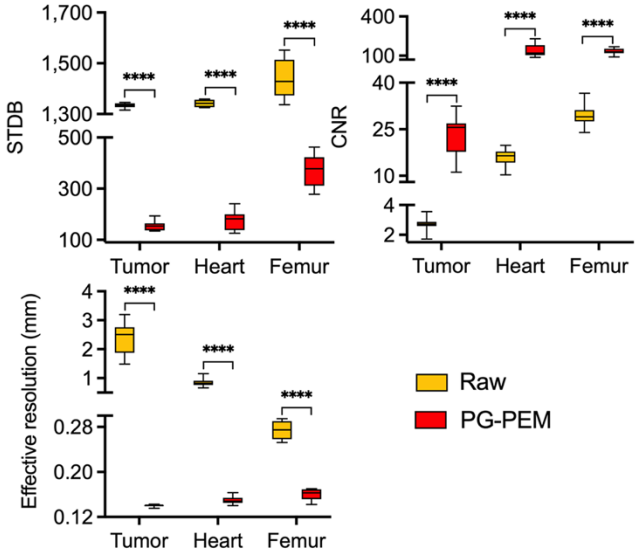

Fig. 4: STDB, CNR and effective resolution assessment of PG-PEM for pre-clinical DAR images.

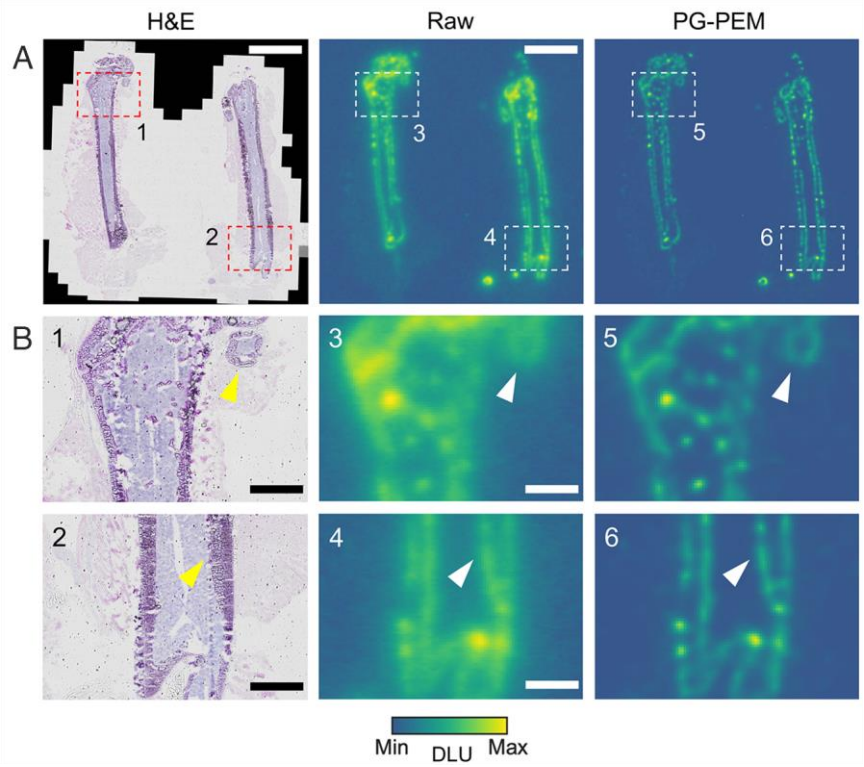

Fig. 5: PG-PEM improves DAR images of ^{18}F-NaF treated femur sections. (A) H&E stained, raw and PG-PEM restored DAR images. (B) Zoomed-in regions of the corresponding boxes in (A). Scale bar: H&E and raw: 5 mm; (B1)–(B4): 1.2 mm.

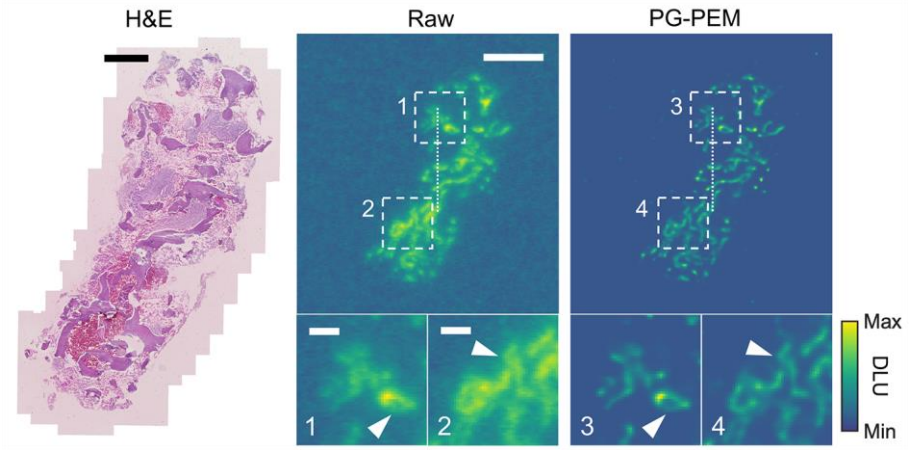

Fig. 6: PG-PEM restoration in alpha particle radiotherapy specimens. From left to right: H&E stained histological image of $^{223}RaCl_2$ treated mCRPC patient bone biopsy, and the corresponding Raw and PG-PEM restored DAR. Scale bar: H&E: 1 mm; Raw: 2.3 mm; Sub-regions (1) and (2): 0.5 mm.

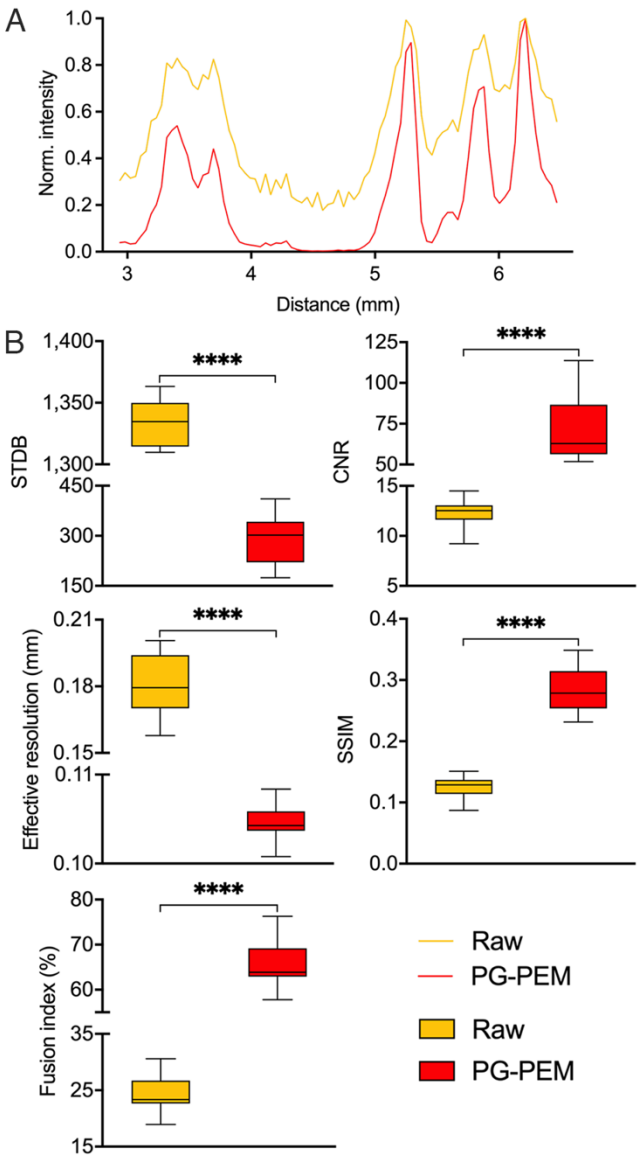

Fig. 7: Quantitative assessment of PG-PEM for the human bone biopsy DAR. (A) Profiles of the dashed lines in Fig. 6. (B) STDB, CNR, effective resolution, SSIM and fusion indices assessment for raw and restored DAR images.

Contents

Supplementary Note 1: PG-PEM algortihm

1.1 DAR imaging model

According to the DAR imaging process, its physical model can be expressed as:

$$R_p = \alpha Q_p + N_p, Q_p \sim \mathcal{P}[(X * h)_p + b_p], N_p \sim \mathcal{N}(0, \sigma_G^2), \tag{S1}$$

where p is the pixel index ($p \in \{1, 2, ..., P\}$), R is the raw DAR image of a tissue, α is a scaling factor corresponding to the gain of the imaging system, X is the "clean" image, h is the PSF, b is the mean of background, $\mathcal{P}[x]$ refers to the Poisson noise with mean x, $\mathcal{N}(0, \sigma_G^2)$ represents Gaussian noise and σ_G is its standard deviation. Because Q and N are both random fields in Eq. (S1), R is also a random field. Thus, we define r as the available observations of R.

According to the definition of Poisson process,

$$\mathcal{P}[(X * h)_p + b_p] = \mathcal{P}[(X * h)_p] + \mathcal{P}[b_p]. \tag{S2}$$

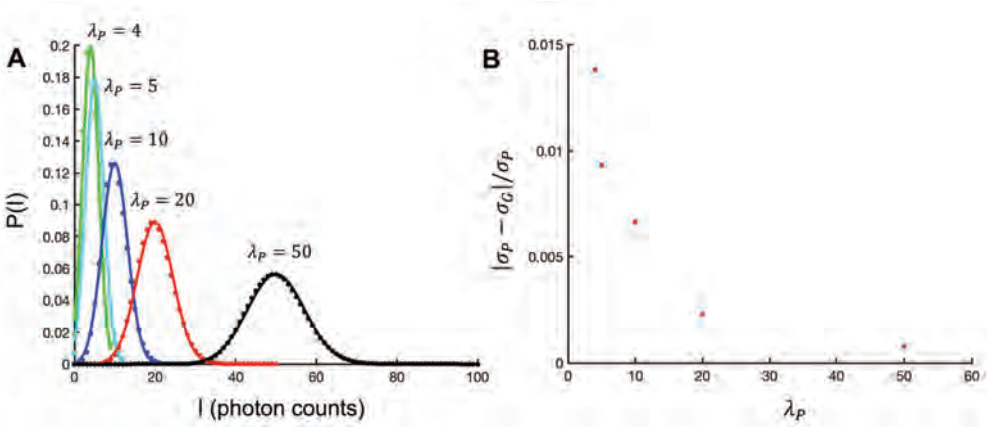

Supplementary Figure 1. Possion distributions approximated as Gaussian distsributions. (A) Poisson-distributed data (dots) for different values of photon flux λ_P and the corresponding Gaussian fitting functions $\mathcal{N}(\lambda_P, \lambda_P)$ (solid lines). **(B)** The relative error between the two distributions, in which σ_P and σ_G are the standard deviation of the Possion- and Gaussian-distributed data, respectively. Based on these results, Poisson distribution can be feasibly approximated as a Gaussian distribution when $\lambda_P > 3$.

When $b > 3$, $\mathcal{P}[b] \approx \mathcal{N}(b, b)$ [1] (Suppmentary Fig. 1). In the DAR images, b is normally assumed to be spatially invariant around the tissue and larger than 3. Therefore, Eq. (S3) is derived from Eqs. (S1) and (S2),

$$\begin{aligned} R &= \alpha \mathcal{P}[X * h] + \alpha \mathcal{N}(b, b) + \mathcal{N}(0, \sigma_G^2) \\ &= \alpha \mathcal{P}[X * h] + \mathcal{N}(\mu_N, \sigma_N^2). \end{aligned} \tag{S3}$$

where $\mu_N = \alpha b$ and $\sigma_N = \sqrt{\alpha^2 b + \sigma_G^2}$. Notably, the raw image can be splitted into Poisson-distributed signal and Gaussian-distributed noise. To estimate the noise parameters μ_N and σ_N, the background part needs to be extracted.

1.2 Patch-based estimation of noise parameters

As Eq. (S3), the raw image can be splitted into Poisson-distributed signal $\alpha\mathcal{P}[X_p * h]$ and Gaussian-distributed noise $\mathcal{N}(\mu_N, \sigma_N^2)$. Because of the unknown true PSF and the non-white noise, the frequency domain-based noise parameters estimation method in [2] cannot be used. To estimate the noise parameters, the background part needs to be extracted. Due to the continuity of the histogram of DAR images (**Supplementary Fig. 2B, H**), simple thresholding method based on intensity values will result in signal pixels aberrantly being classified as background, known as false negative in detection theory. In fact, most of the areas without tissues in DAR images normally should not have radioactive signal from the tissues. Thus, these areas should only have background and noise and be highly similar to each other. Based on this assumption, we propose a patch-based estimation algorithm with Density-Based Spatial Clustering of Applications with Noise [3] (DBSCAN) by searching patches with similar features to robustly estimate the noise parameters. The process is as **Supplementary Algorithm 1** shows.

Supplementary Algorithm 1 Patch-based estimation of noise parameters

Input: Observation of the raw image, r;
Patch size, (M, N);
Output: Mean, αb;
Standard deviation, $\sqrt{\alpha^2 b + \sigma_G^2}$;

1: Split r (**Supplementary Fig. 2A, G**) into multiple patches with size of M rows and N columns (**Supplementary Fig. 2C, I**);
2: Calculate the mean, standard deviation, skewness and kurtosis of every patch;
3: Use the Z-score means method to normalize the data and cluster them by DBSCAN (**Supplementary Fig. 2D, J**);
4: Select the background patches based on the cluster result and form a new dataset: $\{X_p | p = 1, 2, ..., T\}$, where T is the total pixel number of the extracted background;
5: The final values are estimated by MLEM algorithm based on the histograms of the extracted background (**Supplementary Fig. 2E, K**).
6: **return** αb, $\alpha^2 + \sigma_G$.

In this algorithm, M and N are usually set as 10 for our dataset. Besides, it should be noted that when the noise level of the raw image is very high (**Supplementary Fig. 2G**), the corresponding histogram may be cut off at 0 (**Supplementary Fig. 2H**). Under this circumstance, a truncated Gaussian distribution parameters estimation method based on maximum likelihood expectation maximization (MLEM) algorithm is needed [4].

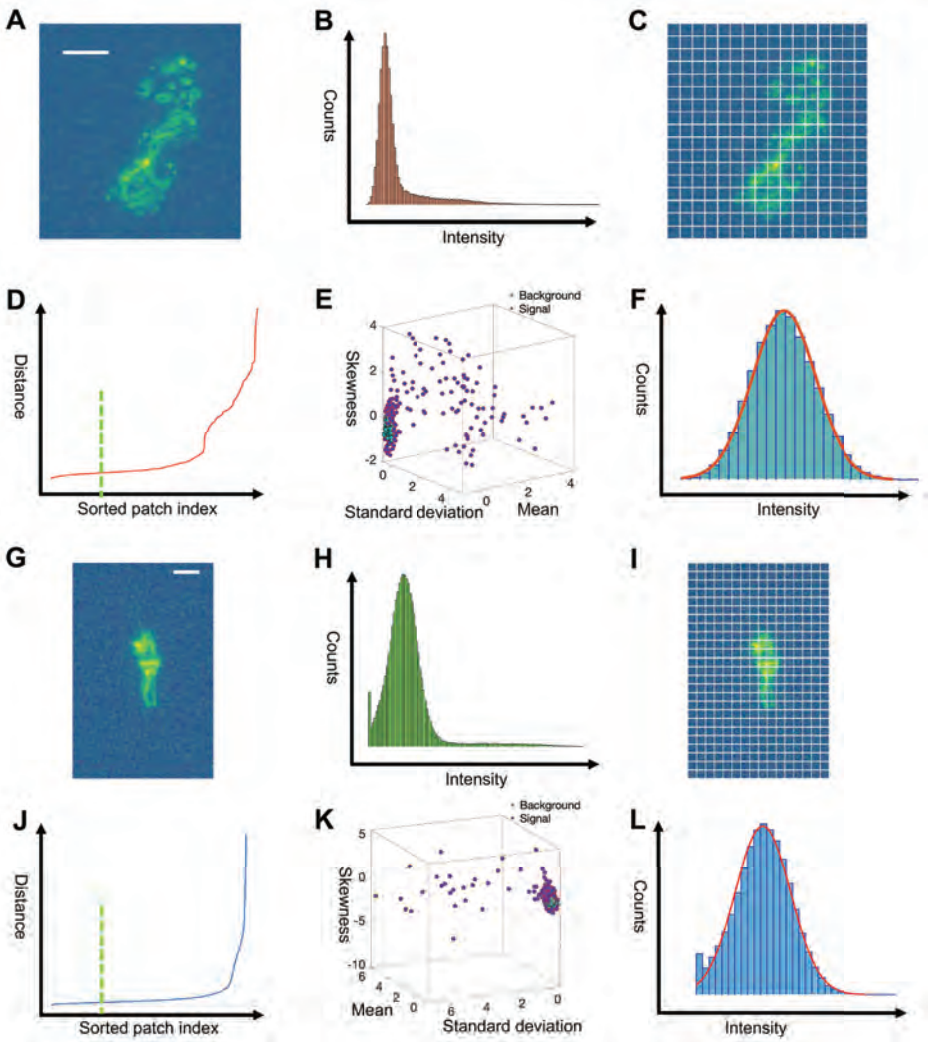

Supplementary Figure 2. Noise parameters estimation. **(A,G)** Raw DAR images with low and high noise levels; **(B,H)** The histogram of the raw images; **(C,I)** Split the raw images into multiple patches and calculate the mean, standard deviation, skewness and kurtosis of each patch; **(E,K)** Plot of the sorted (minPts-1)-th nearest distance of every patch; **(E,K)** DBSCAN results for the patches; **(F,L)** The histograms of the extracted background field which can be fitted by a Gaussian distribution; while **(B)** and **(H)** cannot be. The green dotted lines in **(D)** and **(J)** correspond to the ϵ used in **(E)** and **(K)**. The histogram in **(H)** is truncated at 0 while that in **(B)** is not. To estimate the parameters of the truncated histogram, we apply the truncated MLEM method. Scale bar: **(A)**: 2.3 mm, **(G)**: 4.65 mm.

When implementing DBSCAN, its two parameters ϵ and minPts needs to be manually set, in which ϵ is a parameter specifying the radius of a neighborhood with respect to the same point and minPts is the minimum number of points required to form a dense region. As a rule of thumb, minPts is usually twice as the dimension number of the features. Therefore, we set minPts as 8 in PG-PEM. Meanwhile, we use k-nearest neighbour algorithm to determine ϵ. In detail, a k-distance graph is first built based on the data, and then we find every point's (minPts-1)-th nearest distance, sort them in the order from low to high and plot them (**Supplementary Fig. 2D and J**). Next, unlike the approach [3] which select the "elbow" point as ϵ, we experimentally select the distance before the first 25% position in the range as ϵ, which is far from the "elbow" point for our DAR images. This approach could ensure enough points to form the Gaussian-shape histograms in **Supplementary Fig. 2F and L**. Simultenously, it could also avoid classify signal as background by mistake.

1.3 MLEM algorithm for the mixed Poisson-Gaussian model

By simple variable substitutions using Eq. (S4), Eq. (S3) can be simplified as Eq. (S5), where R' and X are both 2D matrices with P pixels and h is a 2D kernel with S pixels. For our DAR images, normally $S \ll P$.

$$R' = \frac{R}{\alpha}, \mu'_N = \frac{\mu_N}{\alpha} = b, \sigma'_N = \frac{\sigma_N}{\alpha} = \sqrt{b + \frac{\sigma_G^2}{\alpha^2}}, \tag{S4}$$

$$R' = \mathcal{P}[X * h] + \mathcal{N}(b, b + \frac{\sigma_G^2}{\alpha^2}). \tag{S5}$$

Here we donate Q as $\mathcal{P}[X * h]$ and U as $\mathcal{N}(b, b + \frac{\sigma_G^2}{\alpha^2})$, whose elements follow Poisson and Gaussian distributions, respectively. Our goal is to estimate the unknown parameters $\theta = (X, h)$ with the given parameters r' (the available observations of R'), b and $b + \frac{\sigma_G^2}{\alpha^2}$ by following the assumptions for the Poisson-distributed signal and Gaussian-distributed noise in Eq. (S5): 1) they are mutually independent; 2) their components are independent. Under these assumptions, Eq. (S6) is obtained by applying Bayes rule, which is the mixed continuous-discrete probability distribution of (R'_p, Q_p) for every $p \in \{1, 2, ..., P\}$.

$$\begin{aligned} Pr_{R'_p, Q_p}(r'_p, q_p|\theta) &= Pr(Q_p = q_p|\theta) f_{R'_p|Q_p=q_p}(r'_p|b, b + \frac{\sigma^2}{\alpha^2}) \\ &= Pr(Q_p = q_p|\theta) f_{U_p}(r'_p - q_p|b, b + \frac{\sigma^2}{\alpha^2}). \end{aligned} \tag{S6}$$

where $f_{R'_p|Q_p=q_p}(\cdot|b, b+\frac{\sigma^2}{\alpha^2})$ is the conditional probability density function (PDF) of R'_p knowing that $Q_p = q_p$ and $f_{U_p}(\cdot|b, b + \frac{\sigma^2}{\alpha^2})$ is the PDF of U_p. In detail,

$$Pr(Q_p = q_p|\theta) = exp[(-X * h)_p]\frac{(X * h)_p^{q_p}}{q_p!}, \tag{S7}$$

$$f_{U_p}(r'_p - q_p|b, b + \frac{\sigma^2}{\alpha^2}) = \frac{1}{(2\pi)^{1/2}(b + \frac{\sigma_G^2}{\alpha^2})^{1/2}} exp\Big(- \frac{(r'_p - q_p - b)^2}{2(b + \frac{\sigma_G^2}{\alpha^2})}\Big). \tag{S8}$$

Therefore, the likelihood of Eq. (S5) takes the form as Eq. (S9):

$$\begin{aligned} f_{R'}(r'|\theta) &= \prod_{p=1}^{P}\sum_{q_p=0}^{+\infty} Pr_{R'_p,Q_p}(r'_p, q_p|\theta) \\ &= \frac{1}{(2\pi)^{P/2}(b + \frac{\sigma_G^2}{\alpha^2})^{P/2}} \prod_{p=1}^{P} exp[(-X * h)_p] \\ &\sum_{q_p=0}^{+\infty} exp\Big(- \frac{(r'_p - q_p - b)^2}{2(b + \frac{\sigma_G^2}{\alpha^2})}\Big)\frac{(X * h)_p^{q_p}}{q_p!}. \end{aligned} \tag{S9}$$

To solve the parameters θ in Eq. (S9), an iterative MLEM approach is utilized:

$$\theta^{(n+1)} = argmax_\theta J(\theta|\theta^{(n)}), \tag{S10}$$

where $J(\theta|\theta^{(n)}) = E_{Q|R'=r',\theta^{(n)}}[lnPr_{R',Q}(R', Q|\theta)]$ and $Pr_{R',Q}(R', Q|\theta) = \prod_{p=1}^{P} Pr_{R'_p,Q_p}(R'_p, Q_p|\theta)$.

According to Eq. (S6),

$$\begin{aligned} lnPr_{R',Q}(R', Q|\theta) = &-\frac{1}{2(b + \frac{\sigma_G^2}{\alpha^2})^{P/2}} \sum_{p=1}^{P}(R'_p - Q_p - b)^2 - \frac{P}{2} ln(2\pi(b + \frac{\sigma_G^2}{\alpha^2})) \\ &- \sum_{p=1}^{P}(X * h)_p + \sum_{p=1}^{P} ln(X * h)_p Q_p - \sum_{p=1}^{P} ln(Q_p!) \end{aligned} \tag{S11}$$

By dropping the terms that are independent of θ, Eq. (S10) is simplified as:

$$\theta^{(n+1)} = argmin_\theta \tilde{J}(\theta|\theta^{(n)}), \tag{S12}$$

where

$$\tilde{J}(\theta|\theta^{(n)}) = \sum_{p=1}^{N}(X * h)_p - \sum_{p=1}^{N} ln(X * h)_p E_{Q_p|R'_p=r'_p,\theta^{(n)}}(Q_p). \tag{S13}$$

For every $p \in \{1, 2, ..., P\}$, we have

$$\begin{aligned} E_{Q_p|R'_p=r'_p,\theta^{(n)}}(Q_p) &= \sum_{q_p=0}^{+\infty} q_p Pr(Q_p = q_p | R'_p = r'_p, \theta^{(n)}) \\ &= \frac{\sum_{q_p=0}^{+\infty} q_p Pr_{R'_p Q_p}(r'_p, q_p|\theta^{(n)})}{f_{R'_p}(r'_p|\theta^{(n)})} \\ &= \frac{\sum_{q_p=0}^{+\infty} q_p Pr_{R'_p Q_p}(r'_p, q_p|\theta^{(n)})}{\sum_{q_p=0}^{+\infty} Pr_{R'_p, Q_p}(r'_p, q_p|\theta^{(n)})}. \end{aligned} \tag{S14}$$

By combining Eqs. (S6)-(S8), Eq. (S14) simplifies to:

$$E_{Q_p|R'_p=r'_p,\theta^{(n)}}(Q_p) = \frac{\sum_{q_p=1}^{+\infty} exp\Big(- \frac{(r'_p - q_p - b)^2}{2(b+\sigma_G^2/\alpha^2)} \Big) \frac{(X*h)_p^{q_p}}{(q_p-1)!}}{\sum_{q_p=0}^{+\infty} exp\Big(- \frac{(r'_p - q_p - b)^2}{2(b+\sigma_G^2/\alpha^2)} \Big) \frac{(X*h)_p^{q_p}}{q_p!}}. \tag{S15}$$

Therefore, a 2D matrix $E_{Q|R'=r',\theta^{(n)}}(Q)$, sharing the same shape with R' and X, is acquired. When implementing Eq. (S15), there is an issue calculating the infinite terms of q_p on numerator and denominator. Nonetheless, the infinite terms are bounded and the Lambert W function is used to estimate the terms of summarizations, as described previously [5]. The iteration process is done by differentiating Eq. (S13) with respect to X and h and setting the derivative to zero [6–8]. The resulting iterative scheme is given by alternating:

$$\hat{h}^{(n+1)} = \hat{h}^{(n)} \cdot \left[\left(\frac{E_{Q|R'=r',\theta^{(n)}}(Q)}{\hat{h}^{(n)} * \hat{X}^{(n)}} \right) * \hat{X}^{(n),m} \right], \tag{S16}$$

$$\hat{X}^{(n+1)} = \hat{X}^{(n)} \cdot \left[\left(\frac{E_{Q|R'=r',\theta^{(n)}}(Q)}{\hat{h}^{(n)} * \hat{X}^{(n)}} \right) * \hat{h}^{(n),m} \right], \tag{S17}$$

where $\hat{h}^{(n),m}$ and $\hat{X}^{(n),m}$ are the mirrored results of $\hat{h}^{(n)}$ and $\hat{X}^{(n)}$, respectively. In addition, $\hat{h}$ has three constraints: circularly symmetric constraint, non-negativity ($\forall s$, $\hat{h}_s > 0$) and and norm to 1 ($\sum_{s=1}^{S} \hat{h}_s = 1$). To ensure the circularly symmetric constraint, $\hat{h}$ is averaged in the angular direction as Eq. (S18), where r is the magnitude and ϕ is the phase in the polar coordinate system; To ensure $\sum_{s=1}^{S} \hat{h}_s = 1$, Eq. (S19) is conducted; To ensure $\forall s$, $\hat{h}_s > 0$, Eq. (S20) is conducted.

$$\hat{h}'(r) = \frac{1}{2\pi} \int_{-\pi}^{\pi} \hat{h}(rcos\phi, rsin\phi) d\phi. \tag{S18}$$

$$\hat{h} = \frac{\hat{h}'}{\sum_{s=1}^{S} \hat{h}'_s}. \tag{S19}$$

$$\exists \hat{h}_s < 0, \text{set } \hat{h}_s = 0. \tag{S20}$$

1.4 Regularization for h and X

In practice, the blind deconvolution problem is highly ill-posed, so regularizations for both h and X are needed. Through the iteration process h tends to converge as a delta function. To avoid this trivial solution and considering the smooth characteristics of h, h is regularized by L2 norm. The noise of X may amplify in the iteration process, so total variation (TV) is normally added for X [8, 9]. Nevertheless, TV penalty always oversharpens the boundaries between different regions, generating "staircase" effect. To avoid this, we adopted a Hessian Frobenius penalty for the estimated X to enable smoother transitions between different regions and to suppress noise simultaneously [10–12]. As a result, this leads to a penalized MLEM algorithm as Eq. (S21), where λ_h and λ_X are the regularization parameters for h and X, $P_h = exp(-\frac{1}{2}\sum_{s=1}^{S} h_s^2)$ and $P_X = exp(-\sum_{p=1}^{P} |\mathcal{H}X|_p)$ are the prior probability functions for h and X, respectively. Here, $\mathcal{H}$ is a Hessian operator and defined as $[\partial_{xx}, \partial_{xy}; \partial_{xy}, \partial_{yy}]$, where $\partial_{xx} = \partial^2/\partial x^2$, $\partial_{xy} = \partial^2/\partial x \partial y$ and $\partial_{yy} = \partial^2/\partial y^2$. $|\mathcal{H}X|$ is the Hessian Frobenius (HF) norm for X and defined as $\sqrt{(\partial_{xx}X)^2 + (\partial_{yy}X)^2 + 2(\partial_{xy}X)^2}$.

$$\theta^{(n+1)} = argmin_\theta[\tilde{J}(\theta|\theta^{(n)}) + \lambda_h \sum_{s=1}^{S} h_s^2 + 2\lambda_X \sum_{p=1}^{P} |\mathcal{H}X|_p]. \tag{S21}$$

The penalized optimization process for h and X can both be implemented by a forward-backward splitting algorithm similar to [13]. In [13], this algorithm was originally designed for TV regularization. Nevertheless, since the regularization terms for h and X are all convex and the data fidelity term can be extended to a Kullback-Leibler functional without affecting the stationary points [14], which is the same as the condition of TV regularization, the algorithm framework still works for our problem. Therefore, the original Eq. (S16) is modified as EM step and L2 norm regularization step:

$$\begin{cases} \hat{h}^{(n+\frac{1}{2})} = \hat{h}^{(n)} \cdot \left[\left(\frac{E_{Q|R'=r',\theta^{(n)}}(Q)}{\hat{h}^{(n)} * \hat{X}^{(n)}} \right) * \hat{X}^{(n),m} \right] & \text{(EM step)} \\ \hat{h}^{(n+1)} = argmin_h \left\{ \sum_{s=1}^{S} \frac{(\hat{h}_s - \hat{h}_s^{(n+\frac{1}{2})})^2}{\hat{h}_s^{(n)}} + \lambda_h \sum_{s=1}^{S} \hat{h}_s^2 \right\} & \text{(L2 norm regularization step).} \end{cases} \tag{S22}$$

Expand the L2 norm regularization step:

$$\hat{h}^{(n+1)} = argmin_h \left\{ \sum_{s=1}^{S} \frac{1}{\hat{h}_s^{(n)}} \left[\left(1 + \lambda_h \hat{h}_s^{(n)} \right) \hat{h}_s^2 - 2\hat{h}_s^{(n+\frac{1}{2})} \hat{h}_s + const \right] \right\}. \tag{S23}$$

By setting the derivative of every $\hat{h}_s$ to be zero, we get

$$\hat{h}_s^{(n+1)} = \frac{\hat{h}_s^{(n+\frac{1}{2})}}{1+\lambda_h \hat{h}_s^{(n)}}. \tag{S24}$$

Therefore, the solution of Eq. (S22) is

$$\hat{h}^{(n+1)} = \hat{h}^{(n)} \cdot \left[\left(\frac{E_{Q|R'=r',\theta^{(n)}}(Q)}{\hat{h}^{(n)} * \hat{X}_p^{(n)}} \right) * \hat{X}_p^{(n),m} \right] \Big/ \left(1+\lambda_h \hat{h}^{(n)}\right). \tag{S25}$$

Likewise, the original Eq. (S17) is modified as EM step and HF norm regularization step:

$$\begin{cases} \hat{X}^{(n+1)} = \hat{X}^{(n)} \cdot \left[\left(\frac{E_{Q|R'=r',\theta^{(n)}}(Q)}{\hat{h}^{(n)} * \hat{X}^{(n)}} \right) * \hat{h}^{(n),m} \right] & \text{(EM step)} \\ \hat{X}^{(n+1)} = argmin_X \left\{ \sum_{p=1}^{P} \frac{(\hat{X}_p - \hat{X}_p^{(n+\frac{1}{2})})^2}{\hat{X}_p^{(n)}} + 2\lambda_X \sum_{p=1}^{P} |\mathcal{H}\hat{X}|_p \right\} & \text{(HF norm regularization step).} \end{cases} \tag{S26}$$

The HF norm regularization step can be solved by the *majorization−minimization* (MM) framework [10]. Based on this method, the point-wise regularization term can be transformed as Eq. (S27). Its equality holds if and only if $|\mathcal{H}\hat{X}|_p = |\mathcal{H}\hat{X}^{(n)}|_p$, which can be achieved when the iteration converges.

$$|\mathcal{H}\hat{X}|_p \le \frac{|\mathcal{H}\hat{X}^{(n)}|_p}{2} + \frac{|\mathcal{H}\hat{X}|_p^2}{2|\mathcal{H}\hat{X}^{(n)}|_p}. \tag{S27}$$

Thus, minimizing the HF norm regularization step in Eq. (S26) can be conducted by minimizing a surrogate function as Eq. (S28), where $\mathcal{W} = [\partial_{xx}, \partial_{yy}, \sqrt{2}\partial_{xy}]^T$.

$$\hat{X}^{(n+1)} = argmin_X \left\{ \sum_{p=1}^{P} \frac{(\hat{X}_p - \hat{X}_p^{(n+\frac{1}{2})})^2}{\hat{X}_p^{(n)}} + \lambda_X \sum_{p=1}^{P} \frac{|\mathcal{H}\hat{X}|_p^2}{|\mathcal{H}\hat{X}^{(n)}|_p} + const \right\}. \tag{S28}$$

Expanding Eq. (S28), we have:

$$\hat{X}^{(n+1)} = argmin_X \left\{ \sum_{p=1}^{P} \frac{1}{\hat{X}_p^{(n)}} \left[\left(1 + 2\lambda_X \left(\mathcal{W}^T \frac{\mathcal{W}\hat{X}^{(n)}}{|\mathcal{H}\hat{X}^{(n)}|} \right)_p \right) \hat{X}_p^2 - 2\hat{X}_p \hat{X}_p^{n+\frac{1}{2}} + const \right] \right\}. \tag{S29}$$

By setting the derivative of $\hat{X}_p$ to be zero, Eq. (S28) is solved as Eq. (S30), where $\Xi = \frac{\partial}{\partial_{xx}} + \frac{\partial}{\partial_{yy}} + \sqrt{2}\frac{\partial}{\partial_{xy}}$.

$$\hat{X}_p^{(n+1)} = \frac{\hat{X}_p^{(n+1/2)}}{1 + \lambda_X \left(\Xi \frac{\mathcal{W}\hat{X}^{(n)}}{|\mathcal{H}\hat{X}^{(n)}|} \right)_p}. \tag{S30}$$

Therefore, the solution of Eq. (S26) is derived as:

$$\hat{X}^{(n+1)} = \hat{X}^{(n)} \cdot \left[\left(\frac{E_{Q|R'=r',\theta^{(n)}}(Q)}{\hat{h}^{(n)} * \hat{X}^{(n)}} \right) * \hat{h}^{(n),m} \right] \Big/ \left[1 + \lambda_X \left(\Xi \frac{\mathcal{W}\hat{X}^{(n)}}{|\mathcal{H}\hat{X}^{(n)}|} \right) \right]. \tag{S31}$$

1.5 PSF model

The DAR imaging system involves exposing the plate to the radioactive section which produces a latent image through a trapping of electron-hole (**Supplementary Fig. 3A**), and then scanning a laser over the latent image on the phosphor plate to stimulate release of photons (**Supplementary Fig. 3B**). As discussed in the paper, h is circularly symmetric, also affected by the finite focal point of the laser scanner and the modulation transfer function (MTF) of the phospher plate. However, in blind restoration it is not needed to consider all these points to initialize a PSF. Instead, we model it based on the scattering effect using the inverse square law [15]. In **Supplementary Fig. 3A**, the energy of one point in the latent image can be expressed as Eq. (S32), where E_S is the total energy of its source S, E_C is the cut-off energy of the phosphor plate, $d\Omega$ is the unit solid angle corresponding to each pixel. Here, we assume $d\Omega$ is the same for each pixel under the blind restoration framework. As a result, h is approximated as Eq. (S33) when initializing, in which a controls its size. Then its sum is normalized to 1. In fact, because of the regularization for h, the initial value of a does not have a good impact on the result. In our application, we set a as 1.

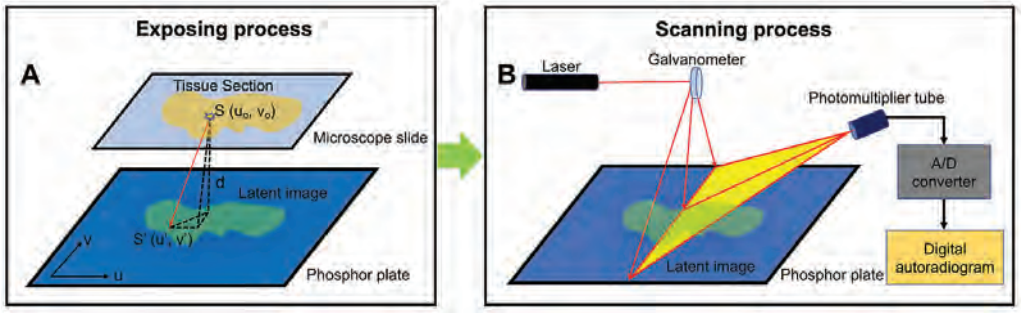

Supplementary Figure 3. DAR imaging process and PSF modelling. (A) Expose the plate to the radioactive section to produce a latent image; **(B)** Scan a laser over the latent image on the phosphor plate to generate the corresponding digital autoradiographic image. d is the distance between the tissue section and the phosphor plate. In uv-plane, the coordinate of S and S' are (u_o,v_o) and (u',v') seperately.

$$E_{S'} = \begin{cases} \frac{E_S}{4\pi[(u'-u_o)^2+(v'-v_o)^2+d^2]} d\Omega & \text{when } E_{S'} > E_C \\ 0 & \text{else} \end{cases}. \tag{S32}$$

$$h = \begin{cases} \frac{1}{a[(u-u_o)^2+(v-v_o)^2]+1} & \text{when } E_{S'} > E_C \\ 0 & \text{else} \end{cases}. \tag{S33}$$

1.6 The impact of the scaling factor α

According to Eqs. (S1), (S4) and (S5), the scaling factor α needs to be pre-calibrated. However, this process is very time-consuming and may not be robust as discussed in the paper. Here, we investigate the impact of α on the restoration result. Assuming α is not calibrated correctly and the calibrated scaling factor is $\alpha^* = \beta\alpha$. Then Eq. (S5) is transformed as Eq. (S34), where X' is the estimated image under this condition.

$$\frac{R'}{\beta} = \mathcal{P}[X' * h] + \frac{\mathcal{N}(b, b + \frac{\sigma_G^2}{\alpha^2})}{\beta}. \tag{S34}$$

By using Poisson distribution to estimate Gaussian distribution, Eq. (S34) is estimated as a shift-Poisson format [12] as Eq. (S35), in which b/β and $(b + \frac{\sigma_G^2}{\alpha^2})/\beta^2$ can both be estimated from R'/β with Algorithm 1.

$$\frac{R' - b}{\beta} + \frac{b + \frac{\sigma_G^2}{\alpha^2}}{\beta^2} = \mathcal{P}[X' * h + \frac{b + \frac{\sigma_G^2}{\alpha^2}}{\beta^2}]. \tag{S35}$$

Based on Eq. (S35), the likelihood of the Poisson statistics is as Eq. (S36), where $k_p = \frac{r'_p - b}{\beta} + \frac{b + \frac{\sigma_G^2}{\alpha^2}}{\beta^2}$ $(p \in \{1, 2, ..., P\})$.

$$f_K(k|\theta) = \prod_{p=1}^{P} exp\left[-(X' * h)_p - \frac{b + \frac{\sigma_G^2}{\alpha^2}}{\beta^2}\right] \frac{\left[(X' * h)_p + \frac{b + \frac{\sigma_G^2}{\alpha^2}}{\beta^2}\right]^{k_p}}{k_p!}. \tag{S36}$$

Therefore, the negative log-likelihood of Eq. (S36) is:

$$-ln f_K(k|\theta) = \sum_{p=1}^{P} \left\{ (X' * h)_p + \frac{b + \frac{\sigma_G^2}{\alpha^2}}{\beta^2} - k_p ln\left[(X' * h)_p + \frac{b + \frac{\sigma_G^2}{\alpha^2}}{\beta^2}\right] + ln(k_p!) \right\}. \tag{S37}$$

By setting the deriative of every $(X' * h)_p$ to be 0, we have:

$$1-\left[(X'*h)_p+\frac{b+\frac{\sigma_G^2}{\alpha^2}}{\beta^2}\right]\Bigg/\left(\frac{r'_p-b}{\beta}+\frac{b+\frac{\sigma_G^2}{\alpha^2}}{\beta^2}\right)=0. \tag{S38}$$

Under the MLEM iterative framework, the result of Eq. (S38) can be expressed as Eq. (S39), where $E(r'_p)$ is the expectation of r'_p.

$$(X'*h)_p=\frac{E(r'_p)-b}{\beta}. \tag{S39}$$

Thus, when the estimated PSF h is the same, the relationship between the results using α^* and α can be approximated as Eq. (S40),

$$X=\beta X'. \tag{S40}$$

Based on these results, the scaling factor α does not have an appreciable impact on the restoration result except as a multiplier parameter β. The reason is that the Gaussian-distributed noise parameters μ_N and σ_N are estimated directly from the background, and this condition is quite similar to that of pure Poisson noise, whose scaling parameter is not required to be calibrated. In fact, digital light unit (DLU) itself is meaningless. When implementing dosimetry calculation, several phantoms should be built for calibrating the mapping relationship between DLU and dosimetry values. In this sense, α will not affect the result of Eq. (S15) and is not needed to be pre-calibrated for DAR image restoration if Eqs. (S34) and (S35) are approximately equal to each other. However, when α^* is too large, the computation process in Eq. (S15) will generate sampling errors, especially for the low intensity regions of the images. To maintain this accurate Gaussian-Poisson (continuous to discrete) transformation, we should make sure $\frac{b+\frac{\sigma_G^2}{\alpha^2}}{\beta^2}=\frac{b}{\beta^2}+(\frac{\sigma_G}{\alpha^*})^2\gg 1$. Therefore, we empirically set $\frac{\sigma_G}{\alpha^*}\geq 10$. In real applications, we can directly use α^* to replace α. Before the restoration process, the raw image could be divided by a large α to decrease the number of summations in Eq. (S15) and then multiply the same α after estimation to maintain the final result with the same scale with the raw image. Then, we set $\alpha\leq\frac{\sigma_G}{10}$. In practice, we set α as $\frac{\sigma_G}{10}$ considering both the computation efficiency and the accuracy of PG-PEM.

1.7 PG-PEM algorithm summary, software availability and runtime analysis

The algorithm is summarized as **Supplmentary Algorithm 2**.

Supplementary Algorithm 2 PG-PEM algorithm

Initialization:

Estimate αb and $\alpha^2 b + \sigma_G^2$ using Algorithm 1.
Rescale r, αb and $\alpha^2 b + \sigma_G^2$ to r', b and $b + \sigma_G^2/\alpha^2$ using the pre-set α and (S4).
Set the raw image observation r' as the initial X.
Initialize the PSF h using Eq. (S33).
Set the regularization parameters λ_X and λ_h.

Iteration:

for each $i = 1, 2, ..., N$ **do**
  E step: Use Eq. (S15) to estimate $E_{Q|R'=r',\theta^{(n)}}(Q)$.
  M step: Use Eq. (S31) to estimate X.
    Use Eq. (S25) to estimate h.
    Use Eqs. (S18), (S19) and (S20) to normalize h.
  if $\sqrt{\sum_{p=1}^{P}(\hat{X}_p^{(n+1)} - \hat{X}_p^{(n)})^2} \Big/ \sqrt{\sum_{p=1}^{P}(\hat{X}_p^{(n)})^2} < threshold$ **then**
    break
  end if
end for

All the codes for PG-PEM were written in Matlab 2019a (MathWorks). The software supporting all proposed methods and example data are available upon reasonable request from the corresponding author.

The runtime of PG-PEM mainly depends on the image size, the number of summation terms in Eq. (S15) and the value of the threshold in Algorithm 2. In our experiments, we typically set the value of the threshold from 0.0005 to 0.001. In such a range, the iteration numbers are usually around 100. Here we report the performance of our software under various image sizes both with and without graphics processing unit (GPU, NVIDIA Quadro RTX 6000) on a workstation using 12 cores Intel(R) Xeon(R) W-2133, 3.60GHz central processing unit (CPU). Specifically, we set the iteration numbers as 100 for all the groups. Besides, the number of summation terms in Eq. (S15) is set as around 700, which can satisfy the criteria in **Supplementary Note 1.6**. The results are presented in **Supplementary Table 1**.

From the table, when the image size is small, CPU-based restoration runs fast. However, as the image sizes grow larger, GPU-based restoration performs better than CPU. Fortunately, the size of all the DAR images utilized in research practice are smaller than 500x500 pixels (pixel size: 0.042x0.042mm^2). Therefore, CPU can fulfill most of the requirements. Notably, PG-PEM could be slower than the algorithm based on the shifted-Poisson model [12] due to the computation of Eq. (S15). Nevertheless, PG-PEM achieves much better denoising

Supplementary Table 1. Computational speed of PG-PEM in different conditions

Image Size (px)	CPU	GPU
250x250	12.3s	42.6s
500x500	85.5s	62.6s
750x750	193.6s	90.7s

performance especially for the images with high noise level. Meanwhile, compared to the very long exposure time of the DAR imaging process (several hours to several days), our PG-PEM algorithm still runs very fast (from several seconds to less than 2 minutes).

Supplementary Note 2: Quality metrics

The root mean squared error (RMSE) is an pixel-wise difference between two input images, where the ideal value is zero. It is computed as Eq. (S41), where Y^{est} is the estimated image, Y^{true} is the ground truth, p is the pixel index and P is the total pixel number for every image.

$$\mathrm{RMSE}(Y^{est}, Y^{true}) = \sqrt{\frac{1}{P}\sum_{p=1}^{P}(Y_p^{est} - Y_p^{true})^2} \tag{S41}$$

The signal power to noise power ratio (SNR) indicates the ratio of the power of a signal to the power of background noise. It is defined as Eq. (S42), where Y^{est} is the estimated image from restoration algorithms and Y^{true} is the ground truth.

$$\mathrm{SNR}(Y^{est}, Y^{true}) = 10log\frac{\sum_{p=1}^{P}(Y_p^{true})^2}{\sum_{p=1}^{P}(Y_p^{est} - Y_p^{true})^2} \tag{S42}$$

The structure similarity [16] (SSIM) is a perception-based model that considers image degradation as perceived change in structural information, while also incorporating important perceptual phenomena, including both luminance masking and contrast masking terms. Compared to RMSE and SNR, it is supposed to give more information about image distortion by the computation of local image structure, luminance and contrast into a single local quality score. In this paper, the luminance and contrast are normalized and SSIM is defined as Eq. (S43),

$$\mathrm{SSIM}(Y^{est}, Y^{true}) = \frac{2\mu_{Y^{est}}\mu_{Y^{true}} + C_1}{\mu_{Y^{est}}^2 + \mu_{Y^{true}}^2 + C_1} \cdot \frac{2\sigma_{Y^{est}Y^{true}} + C_2}{\sigma_{Y^{est}}^2 + \sigma_{Y^{true}}^2 + C_2} \tag{S43}$$

where Y^{est} is the estimated image from restoration algorithms, Y^{true} is the ground truth, $\mu_{Y^{est}}$, $\mu_{Y^{true}}$, $\sigma_{Y^{est}}$, $\sigma_{Y^{true}}$ and $\sigma_{Y^{est}Y^{true}}$ are the local means, standard deviations and cross-covariance for images Y^{est} and Y^{true}, C_1 and C_2 are the regularization constants to avoid instability for image regions where the local mean or standard deviation is close to zero.

Contrast to noise ratio (CNR) is defined as Eq. (S44),

$$\mathrm{CNR} = (C_{sig} - C_{bg})/\sigma_{bg} \tag{S44}$$

where C_{sig} and C_{bg} are the mean of the signal and background and σ_{bg} is the standard deviation of the background. In this metric, the signal area is defined as the high activity region in the DAR images, and the background is extracted by our patch-based estimation method.

Effective resolution is estimated based on the recently published decorrelation-based method [17]. This method estimates the highest frequency with sufficiently high signal in relation to noise (**Supplementary Fig. 4**).

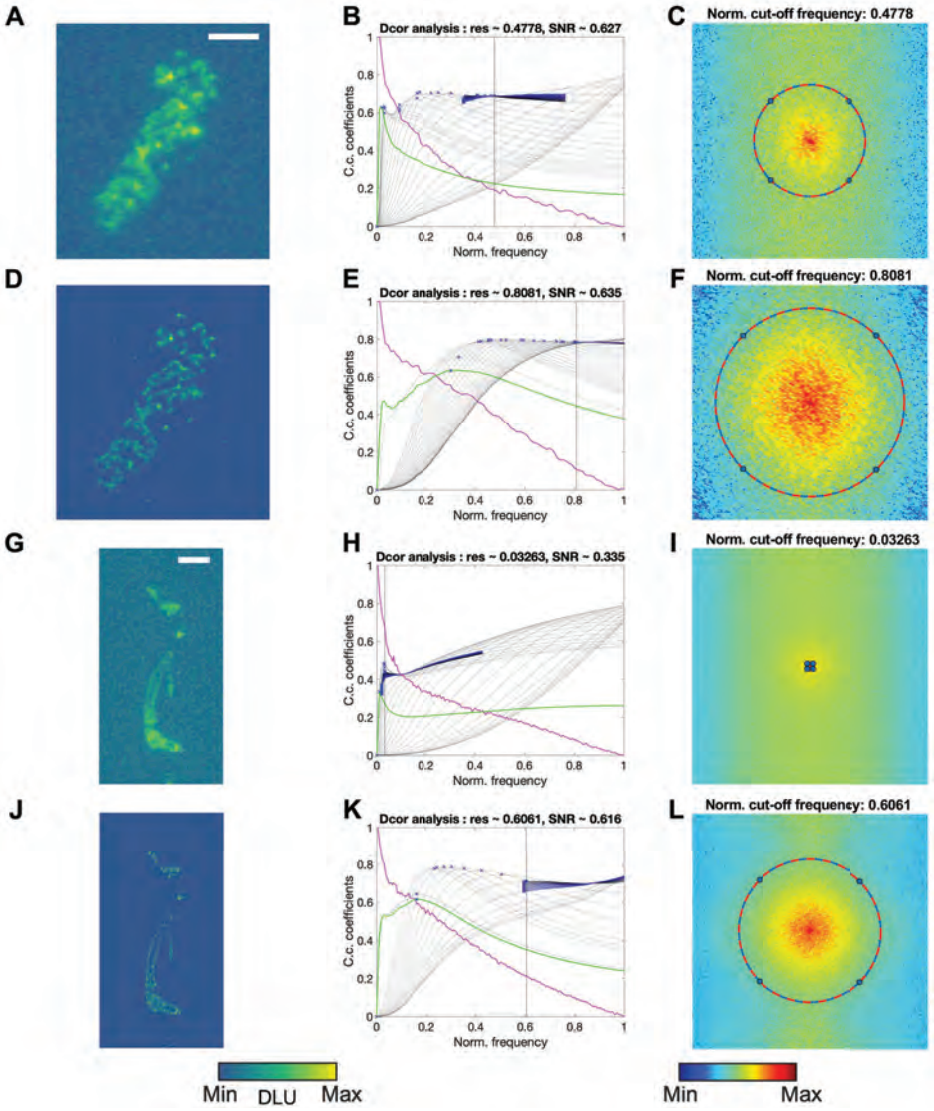

Supplementary Figure 4. Effective resolution estimation by decorrelation analysis. **(A,G)** Two Raw DAR images with low and high noise levels, respectively. **(D,J)** The corresponding PG-PEM restored images of **A** and **G**. **(B,E,H,K)** The corresponding decorrelation analysis of **(A)**,**(D)**,**(G)** and **(J)**. **(C,F,I,L)** The log-scale frequency map of **(A)**,**(D)**,**(G)** and **(J)** labeled with cut-off frequency estimated from **(B)**,**(E)**,**(H)** and **(K)**, respectively. Scale bar: **(A)**: 1.8 mm. **(B)**: 5.3 mm.

Supplementary Note 3: Reference methods

We modified five restoration algorithms as referenced to blind restore DAR images, namely Richardson-Lucy (RL) [6], RL with wavelet-based residue denoising (RD) [18], Shift-Poisson (SP) [12], PG-PEM with no regularization for X (NP) and PG-PEM with TV regularization (TV).

3.1 RL algorithm

RL algorithm is fit for Poisson-distributed data. For DAR image restoration problem, it assumes the imaging model is:

$$R = \alpha \mathcal{P}[X * h + b]. \tag{S45}$$

Based on this model, Eq. (S46) demonstrates the iterative deconvolution scheme without regularization.

$$\begin{aligned} \hat{h}^{(n+1)} &= \hat{h}^{(n)} \cdot \left[\left(\frac{r'}{\hat{h}^{(n)} * \hat{X}^{(n)} + b} \right) * \hat{X}^{(n),m} \right], \\ \hat{X}^{(n+1)} &= \hat{X}^{(n)} \cdot \left[\left(\frac{r'}{\hat{h}^{(n)} * \hat{X}^{(n)} + b} \right) * \hat{h}^{(n),m} \right]. \end{aligned} \tag{S46}$$

3.2 RD algorithm

Different from RL, RD algorithm performs residual denoising during each iteration. In [7, 8], the authors utlized median filter as the denoising algorithm. Not the same as them, wavelet denoising algorithm [18] is applied here. The basic scheme of RD is as Eq. (S47), where $Denoise()$ represents wavelet denoising algorithm.

$$\begin{aligned} r'^{(n)} &= r' - \hat{h} * \hat{X}^{(n)}, \\ \overline{r'^{(n)}} &= Denoise(r'^{(n)}), \\ \hat{h}^{(n+1)} &= \hat{h}^{(n)} \cdot \left[\left(\frac{\hat{h}^{(n)} * \hat{X}^{(n)} + \overline{r'^{(n)}}}{\hat{h}^{(n)} * \hat{X}^{(n)} + b} \right) * \hat{X}^{(n),m} \right], \\ \hat{X}^{(n+1)} &= \hat{X}^{(n)} \cdot \left[\left(\frac{\hat{h}^{(n)} * \hat{X}^{(n)} + \overline{r'^{(n)}}}{\hat{h}^{(n)} * \hat{X}^{(n)} + b} \right) * \hat{h}^{(n),m} \right]. \end{aligned} \tag{S47}$$

In the wavelet denoising algorithm, the input image is decomposed for 7 levels, and Stein's Unbiased Risk Estimate (SURE) and a soft-thresholding approach are conducted.

3.3 SP algorithm

As discussed in Section 1.6, Eq. (S5) can be transformed to a shifted-Poisson distribution:

$$R' + \frac{\sigma_G^2}{\alpha^2} = \mathcal{P}[X * h + b + \frac{\sigma_G^2}{\alpha^2}]. \tag{S48}$$

Based on this equation, the iteration scheme can be conducted as Eq. (S49).

$$\begin{aligned} \hat{h}^{(n+1)} &= \hat{h}^{(n)} \cdot \left[\left(\frac{r' + \frac{\sigma_G^2}{\alpha^2}}{\hat{h}^{(n)} * \hat{X}^{(n)} + b + \frac{\sigma_G^2}{\alpha^2}} \right) * \hat{X}^{(n),m} \right], \\ \hat{X}^{(n+1)} &= \hat{X}^{(n)} \cdot \left[\left(\frac{r' + \frac{\sigma_G^2}{\alpha^2}}{\hat{h}^{(n)} * \hat{X}^{(n)} + b + \frac{\sigma_G^2}{\alpha^2}} \right) * \hat{h}^{(n),m} \right]. \end{aligned} \tag{S49}$$

3.4 NP and TV algorithms

Note that NP and TV have almost the same framework with PG-PEM except the regularization for X. We aim to show the competitive performance of Hessian Frobenius norm regularization in DAR images by comparing it with NP and TV. NP does not have regularization for X while TV algorithm utilizes TV norm as its regularization for X as Eq. (S50), in which $\bigtriangledown$ represents $[\frac{\partial}{\partial x}, \frac{\partial}{\partial y}]$ and $div = \frac{\partial}{\partial x} + \frac{\partial}{\partial y}$.

$$\hat{X}^{(n+1)} = \hat{X}^{(n)} \cdot \left[\left(\frac{E_{Q|R'=r',\theta^{(n)}}(Q)}{\hat{h}^{(n)} * \hat{X}_p^{(n)}} \right) * \hat{h}^{(n),m} \right] \Big/ \left[1 - \lambda_X div \left(\frac{\bigtriangledown \hat{X}^{(n)}}{|\bigtriangledown \hat{X}^{(n)}|} \right) \right]. \tag{S50}$$

3.5 Regularization strategies for the reference methods

RL, RD and SP have the same regularization strategies for both h and X with PG-PEM, while NP and TV have the same regularization stragegy for h. Further, similar to PG-PEM, the scaling parameter α here does not impact the estimation result except a multiplier parameter.

Supplementary Note 4: Simulations

4.1 Simulated data generation

We use Eq. (S51) to generate simulated data, in which p is the pixel index, X the ground truth, h the pre-set PSF, b the background, α the scaling factor and $\mathcal{N}(0, \sigma_G^2)$ the Gaussian noise with mean of 0 and standard deviation of σ_G. Here, α and σ_G control the level of Poisson and Gaussian noises, respectively. Note that we divide $X * h + b$ with α to ensure the generated images with the same range with the ground truth.

$$R = \alpha \mathcal{P}\left[\frac{X * h + b}{\alpha}\right] + \mathcal{N}(0, \sigma_G^2) \tag{S51}$$

Because it is impossible to acquire a "clean" raw DAR image without noise and blurring effect, the ground truth image needs to be generated. To do so, we selected a raw DAR image with low noise level and blurring effect. Then, it was blindly restored by PG-PEM. The regularization parameters were carefully tuned so that the restored image could achieve its best quality. After restoration, the background of the image was cleared to further remove background noise. The pre-set PSF was generated using a more blurred raw DAR image so that the kernel size of the PSF is larger. To do this, we aim to better test the deblurring ability of the restoration algorithms. The generated ground truth image and PSF are both shown in **Supplementary Fig. 5A**.

4.2 Characterization of the regularization parameters of PG-PEM

To test the impact of regularization parameters, different λ_X (0 to 0.1) and λ_h (0 to 10) were selected to test the performance of the algorithm using a simulated image. To generate the image, the ground truth image was convoluted with the pre-set PSF, to which a constant background was added (b=4000) and then corrupted with Poisson noise (α=20) and Gaussian noise with standard deviation (σ_G) of 1500. The generated image (**Supplementary Fig. 5C**) was restored using the PG-PEM algorithm with the different regularization parameters. The results are shown in **Supplementary Fig. 5D-L**. Meanwhile, several restoration results and their corresponding PSFs with different regularization parameters are shown in **Supplementary Fig. 6**. Here, RMSE, SSIM and SNR are set as the accuracy metrics.

From **Supplementary Fig. 5**, the regularization parameters indeed increases the restoration accuracy compared to the condition without regularizations. The results are very similar across the range of λ_h. For example, in **Supplementary Fig. 5E**, the optimal value for λ_h is approximately 1.2, but the results are very close to each other when λ_h is in [0.7, 1.7]. On the contrary, in **Supplementary Fig. 5F**, the optimal value for λ_X is in a narrow range of approximately 0.0005 to 0.0015. In fact, λ_X should be a small value so as to keep the

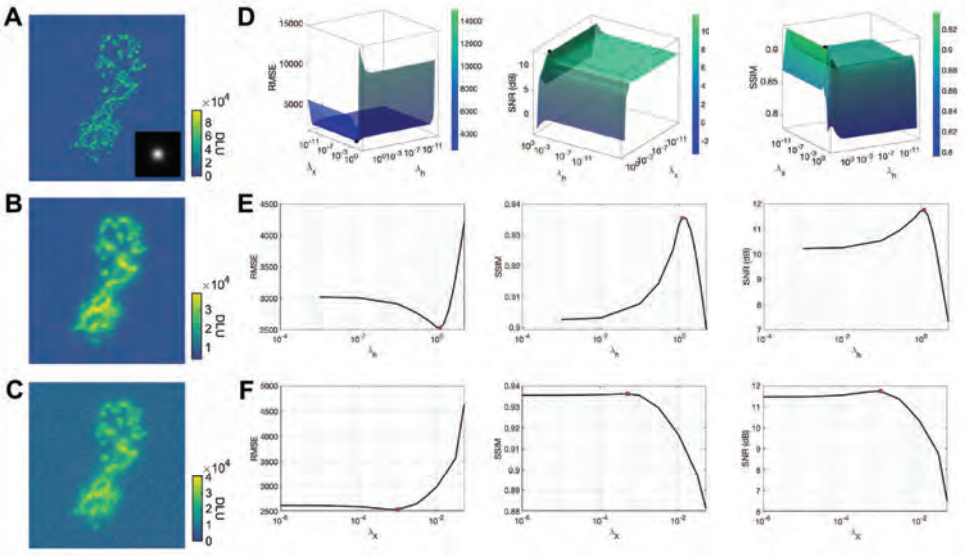

Supplementary Figure 5. Data generation for simulation and accuracy metrics for different parameters. **(A)** Ground truth image and corresponding PSF; **(B)** Blurred image with background; **(C)** Noisy image; **(D)** RMSE, SSIM and SNR for all the parameters; **(E)** RMSE, SSIM and SNR with different λ_h when $\lambda_X = 0.001$; **(F)** RMSE, SSIM and SNR with different λ_X when $\lambda_h = 1.2$. Note that in the figures the dots indicate the optimal values.

estimated X from being over-smoothed.

From **Supplementary Fig. 6**, the parameters λ_h and λ_X control the strength of regularization on the PSF h and specimen image X, respectively. With larger λ_X, the restored images tend to become less noisy. But when it is large enough, the restored images will lose fine details and become blurry. Therefore, it is essential to set λ_X properly in order to restore the raw images with a good quality. Combined with the conclusion from **Supplementary Fig. 6**, λ_X is experimentally set as a small value around 0.001 to suppress the noise while preserving the resolution simultaneously. When λ_h=0, the kernel size of h is very small, indicating the estimated h tends to converge as a delta function in this condition. As λ_h increases, the kernel size of the estimated h becomes larger, and the restored image becomes less noisy and blurry. This validates that the regularization is able to ensure its smoothness and to prevent h from converging to a delta function. However, when λ_h is large enough, parts of the restored images become over-smoothed. In this case, the restored images lose some details due to the over-estimated h. This phenomenon can be interpreted in frequency domain (k-space). When λ_h is smaller, the corresponding optical transfer function (OTF) in k-space is broader. Therefore, there will be more high frequency noises and the restoration results are not ideal. On the contrary, when λ_h is larger, the OTF is narrower. As a result, more high frequency signal is filtered out and X looks more blurry. In this sense, the regularization strategy for h is very similar to a Wiener filter. Because λ_h impacts the size of the OTF, it should be positively

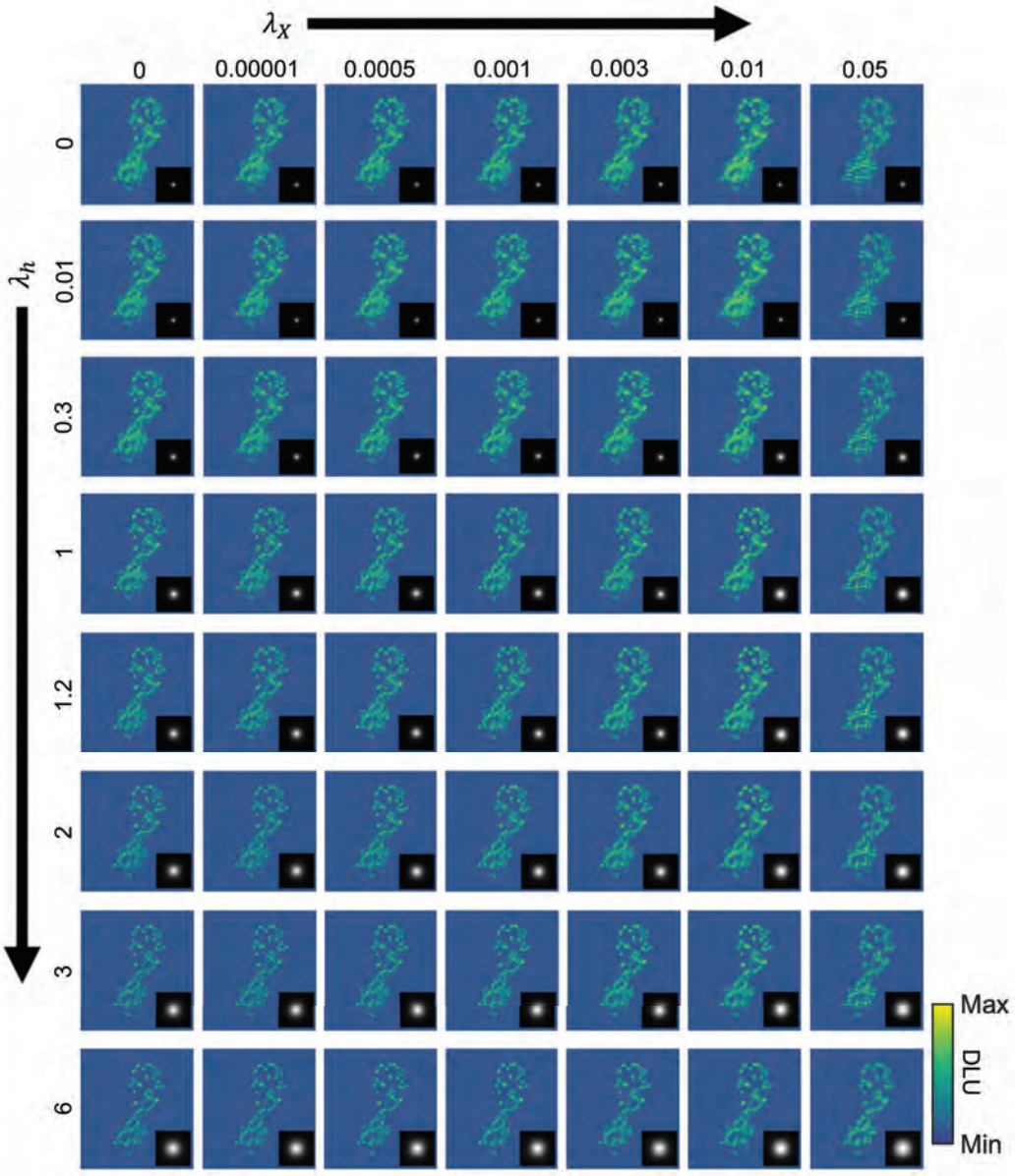

Supplementary Figure 6. Restoration images and corresponding PSFs using PG-PEM algorithm with λ_h from 0 to 10 and λ_X from 0 to 0.1. With λ_h increasing, the kernel size of the estimated PSF become larger and larger, and the restored images tend to become less noisy. But when the PSF kernel is large enough, the restored images become blurry. With λ_X increasing, the image noise is also suppressed. But with too large λ_X, the images lose fine details and become blurry.

correlated to the noise level of the input images. For our DAR images, the parameter λ_h is normally set between 0 and 4, determined by the noise level of the input images. In our work, we use the reciprocal of the CNR of the images to reflect their noise levels.

$$\text{Noise level} = \sigma_{bg}/(C_{sig} - C_{bg}), \tag{S52}$$

where C_{sig} and C_{bg} are the mean of the signal and background and σ_{bg} is the standard deviation of the background. The same is done for CNR; the signal area is defined as the high activity region in the DAR images, and the background is extracted by our patch-based estimation method. Reasonably, this can reflect the normalized noise after considering both the noise power and the averaged signal energy. We also found that λ_h grows slower with the noise level increasing because the E step in Eq. (S15) can also suppress parts of the noise. We thus emperically set λ_h as:

$$\lambda_h = 4\sqrt{\text{Noise level}}. \tag{S53}$$

In fact, according to the results in **Supplementary Fig. 5 and 6**, the restored data are quite similar along a range of λ_h, which brings more flexibility to our empirical setting of λ_h in Eq. (S53). We can further tune the λ_h manually, for example, by visual assessment or with the help of the decorrelation analysis method [17]. The most optimal λ_h should correspond to the point with the best signal-noise trade-off.

4.3 Comparison with the reference algorithms

Next, to evaluate the denoising performance of PG-PEM algorithm, the simulated image had added to it a constant background (b=4000), blurred by the same PSF again and corrupted with two different levels of Poisson noise (α=20 and 100) and Gaussian noise with different standard deviations (σ_G) from 0 to 3000 with interval of 500. We generated 10 groups of data for each noise level. In this way, by generating simulated images with different Poisson and Gaussian noise levels, we aim to have a thorough comparison of the algorithms under different conditions.

The PG-PEM algorithm was compared with RL, RD, SP, NP and TV. In this simulation, λ_X is set as 0.001. RL, RD and SP shared the same λ_X but different λ_h to make sure the PSFs of these algorithms have the same shape. We did this to eliminate the impact of PSF and only focused on the different frameworks of these models. RMSE, SSIM and SNR were used to compare the restoration performance between different algorithms. The results are shown in **Supplementary Fig. 7**.

$$R' = \mathcal{P}[X * h] + \gamma\mathcal{P}(b/\gamma) \tag{S54}$$

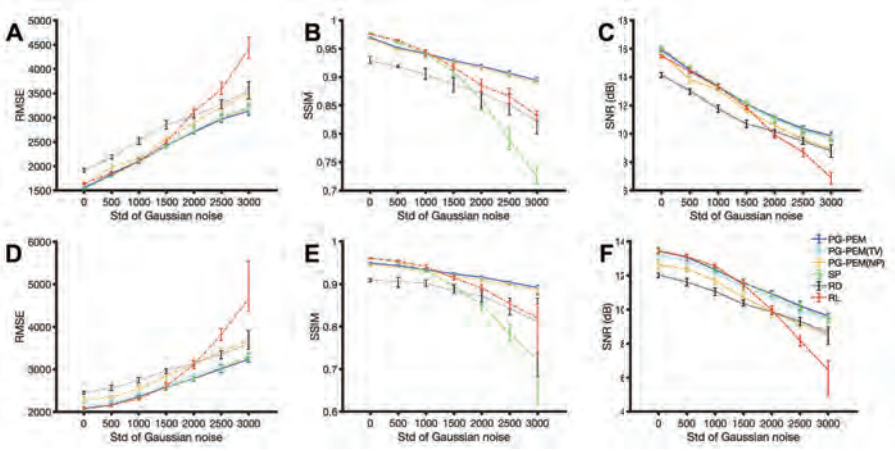

Supplementary Figure 7. Evaluation results for different parameters and methods when α=20 and 100. **(A)** RMSE evaluation when α=20; **(B)** SSIM evaluation when α=20; **(C)** SNR evaluation when α=20; **(D)** RMSE evaluation when α=100; **(E)** SSIM evaluation when α=100; **(F)** SNR evaluation when α=100. From the figures, PG-PEM is the best performer among all the conditions regarding RMSE, SSIM and SNR.

From **Supplementary Fig.** 7, in the parametric space where the standard deviation of the Gaussian noise is small, RL outperforms RD and is similar to SP and PG-PEM. However, with additional noise, RD algorithm performs better than RL. This can be interpreted using Eq. (S54) estimated from Eq. (S5), where $(\gamma-1)b = \sigma_G^2/\alpha^2$. When σ^2 is small, the Gaussian noise part can be approximated as a Poisson distribution; while σ^2 is large enough, the Gaussian distribution will be truncated. Therefore, the approximation will cause large errors. This is why as Gaussian noise increases above a level, the performance of RL decreases dramatically. In aspects of RMSE and SNR, the performances of SP and PG-PEM are comparable, both of which are not worse than those of RL and RD. When the level of Gaussian noise is higher, the SSIM of PG-PEM is much better than that of SP. Next, NP, TV and PG-PEM were compared to evaluate the different regularization strategies for X. For all the conditions with different noise levels, PG-PEM always outperforms TV and NP is the worst of all. In summary, PG-PEM is the best performer in aspects of RMSE, SSIM and SNR for simulated image data restoration. Parts of the restored images with their log-scale versions are shown in **Supplementary Figs.** 8-11. The same as the results from the accuracy metrics, PG-PEM outperforms alternative methods by means of visual inspection.

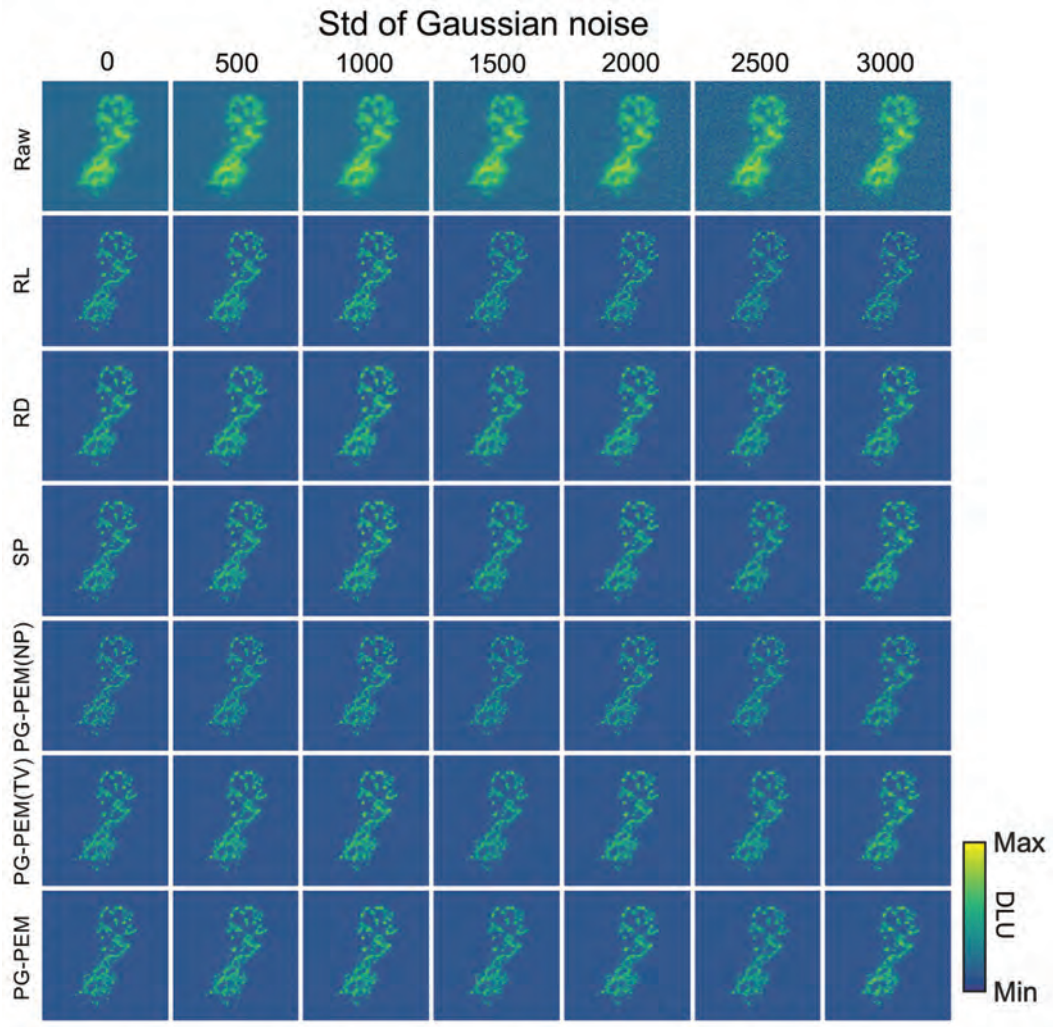

Supplementary Figure 8. Restoration results from different noise levels and methods when α=20.

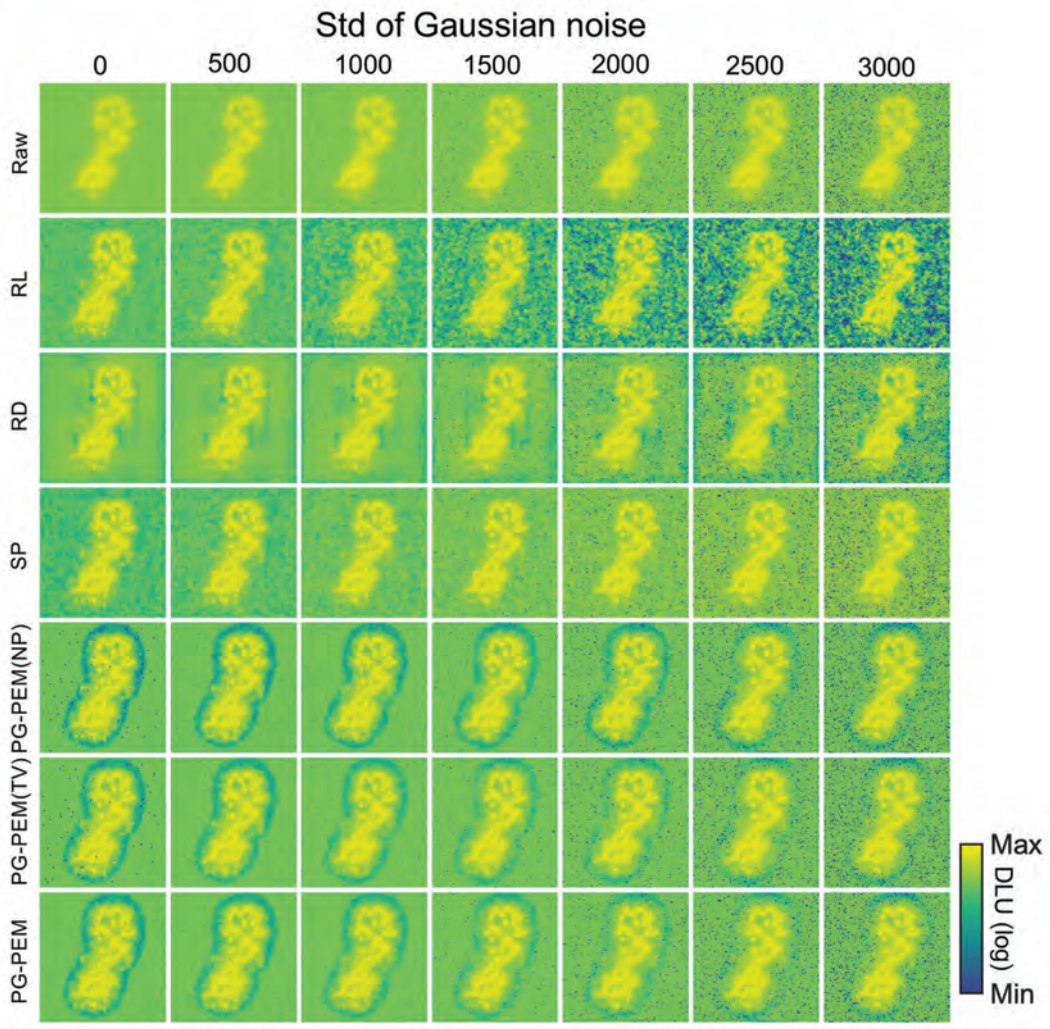

Supplementary Figure 9. Restoration results from different noise levels and methods when α=20 (log scale). It is easier to compare the denoising ability between different methods using the log-scale images.

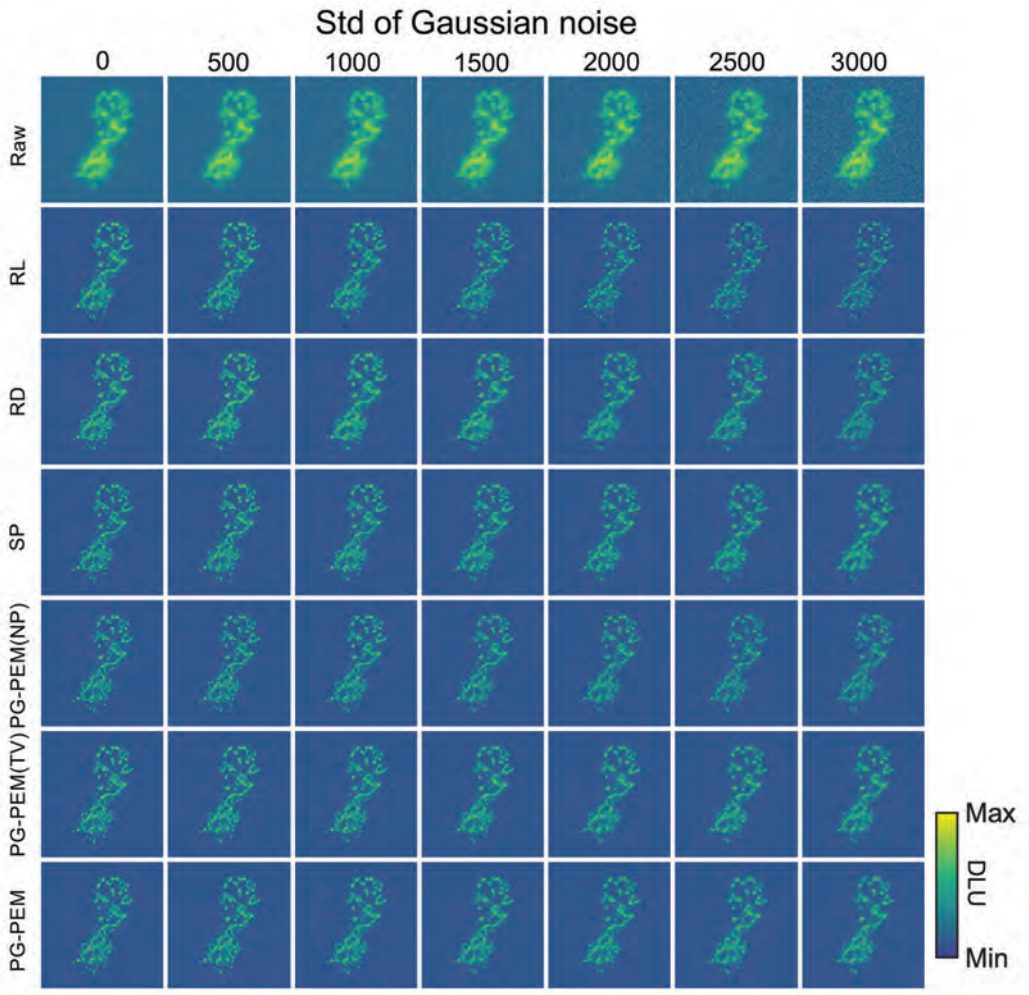

Supplementary Figure 10. Restoration results from different noise levels and methods when α=100.

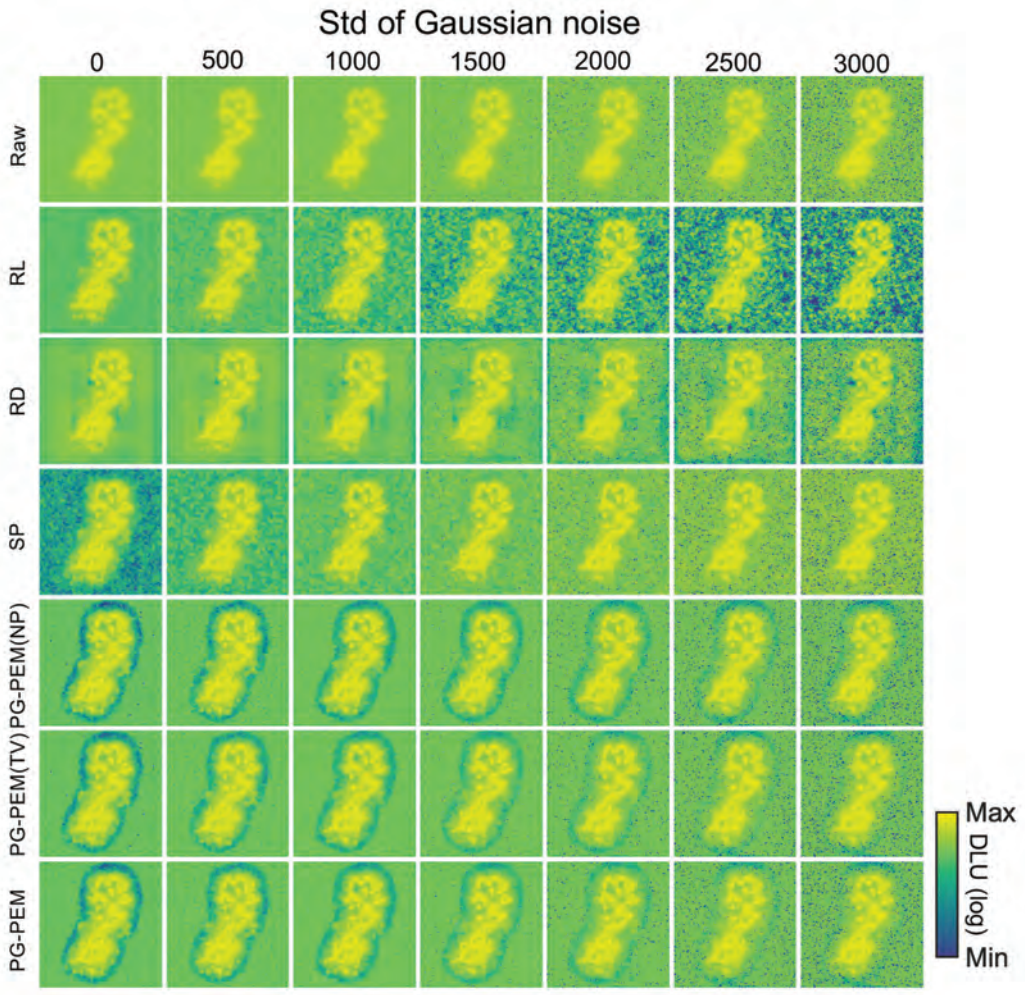

Supplementary Figure 11. Restoration results from different noise levels and methods when α=100 (log scale). It is easier to compare the denoising ability between different methods using the log-scale images.

Supplementary Figures 12-21

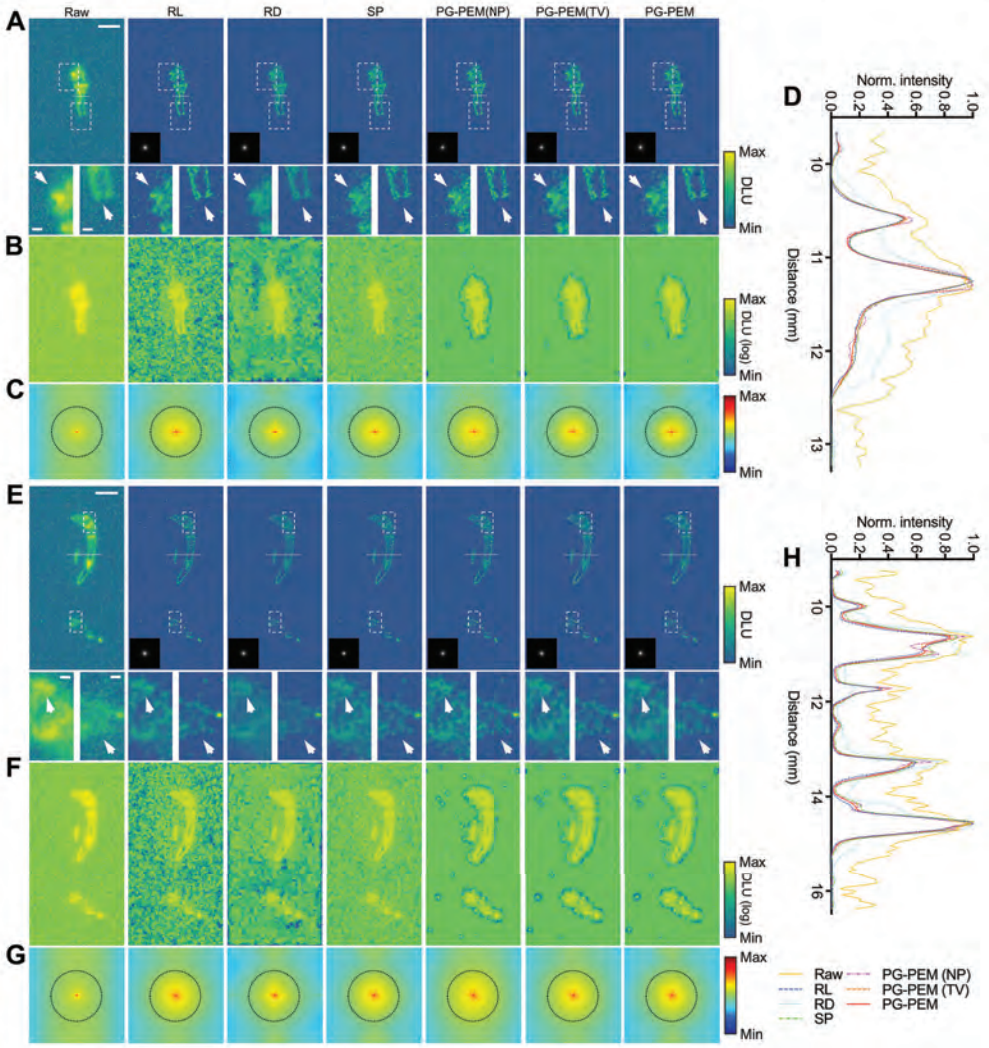

Supplementary Figure 12. Assessment of PG-PEM in comparison with alternative blind restoration algorithms. **(A,E)** Raw DAR images from the mouse hindlimb following [^{18}F]NaF PET imaging and the restoration results with the corresponding PSFs using modified restoration algorithms, PSF estimation and patch-based segmentation. The corresponding estimated PSFs are inset by grayscale. The lower images are the magnificiation of dash-outlined regions from the raw and restored images in **(A,E)**. **(B,F)** Log-scale transformed images from **(A,E)** for background appraisal. **(C,G)** Log-scale magnitude of the Fourier transform of the raw and restored images in **(A,E)**, respectively. **(D,H)** Line profiles of the images in **(A,E)** along the corresponding dashed lines. Scale bar: **(A)**: upper images: 4.7 mm, lower images: 1.4 mm. **(E)**: upper images: 4.85 mm, lower images: 0.59 mm.

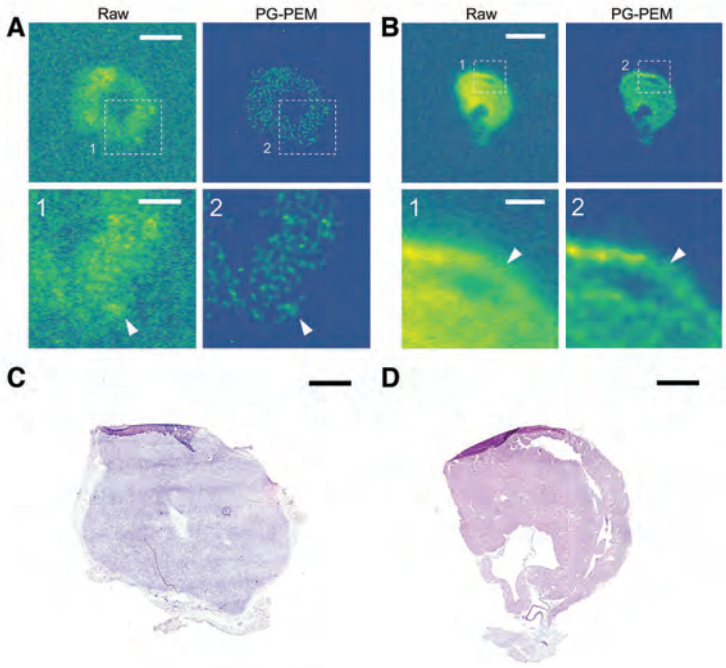

Supplementary Figure 13. Content-adaptive blind restoration improves preclinical DAR. (A), (B) Raw and PG-PEM restored DAR images of mice tumor and heart treated with ^{18}F-FDG. **(C), (D)** The corresponding H&E stained tumor and heart tissues. Scale bar: **(A)**: 4.2 mm, **(A1)**: 1.4 mm; **(B)**: 3.7 mm, **(B1)**: 0.75 mm; **(C)**: 1.5 mm; **(D)**: 1.25 mm.

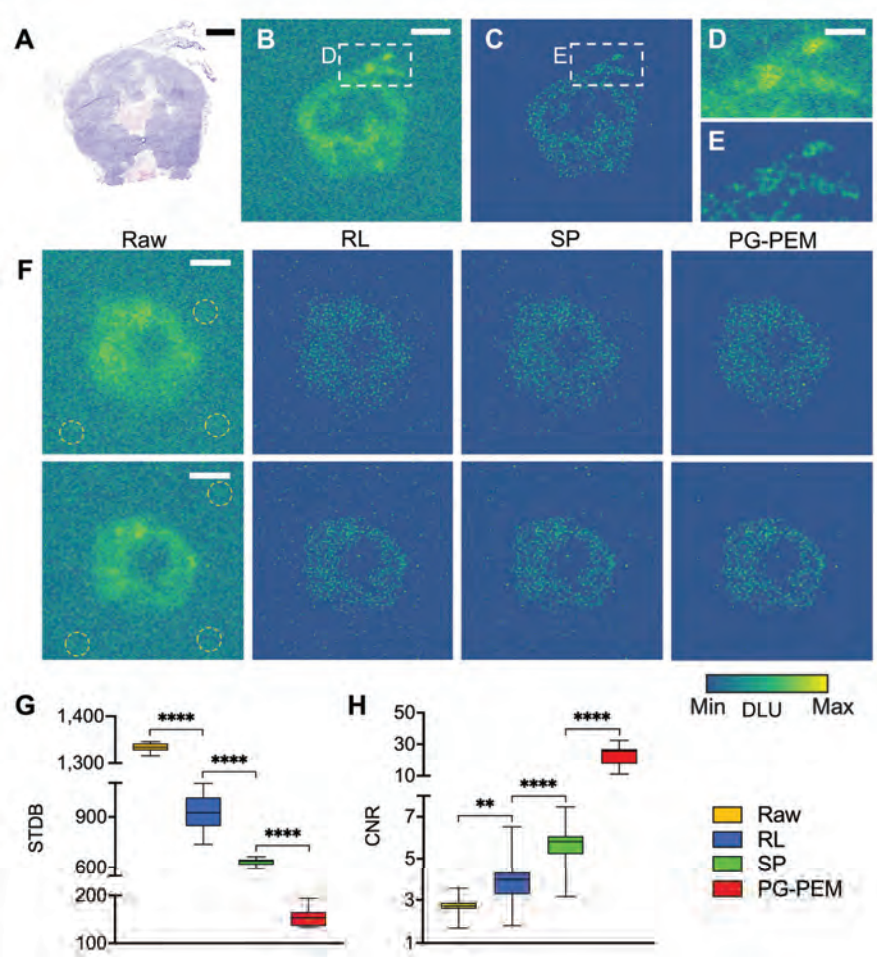

Supplementary Figure 14. PG-PEM outperforms RL and SP in the restoration of raw DAR images from [^{18}F]FDG uptake by xenograft tumors. **(A)** A H&E stained tumor tissue image. **(B)** The corresponding raw DAR image of **(A)**. **(C)** The restored image of **(B)** using PG-PEM. **(D,E)** Magnified regions of the two dashed areas in **(B,C)**. **(F)** Another two groups of raw DAR images with the corresponding restored results using RL, SP and PG-PEM. By observing the dashed yellow circles in the raw images and the corresponding regions in the restored results of RL, SP and PG-PEM, PG-PEM can effectively suppress the noise in the circles while RL and SP cannot. **(G,H)** STDB and CNR assessment of totally 10 groups of DAR images. These results demonstrate that PG-PEM performs significantly better than RL and SP in denoising. Scale bar: **(A)**: 2 mm. **(B)**: 3.6 mm. **(D)**: 1.5 mm. **(F)**: first row: 3.3 mm, second row: 3.28 mm.

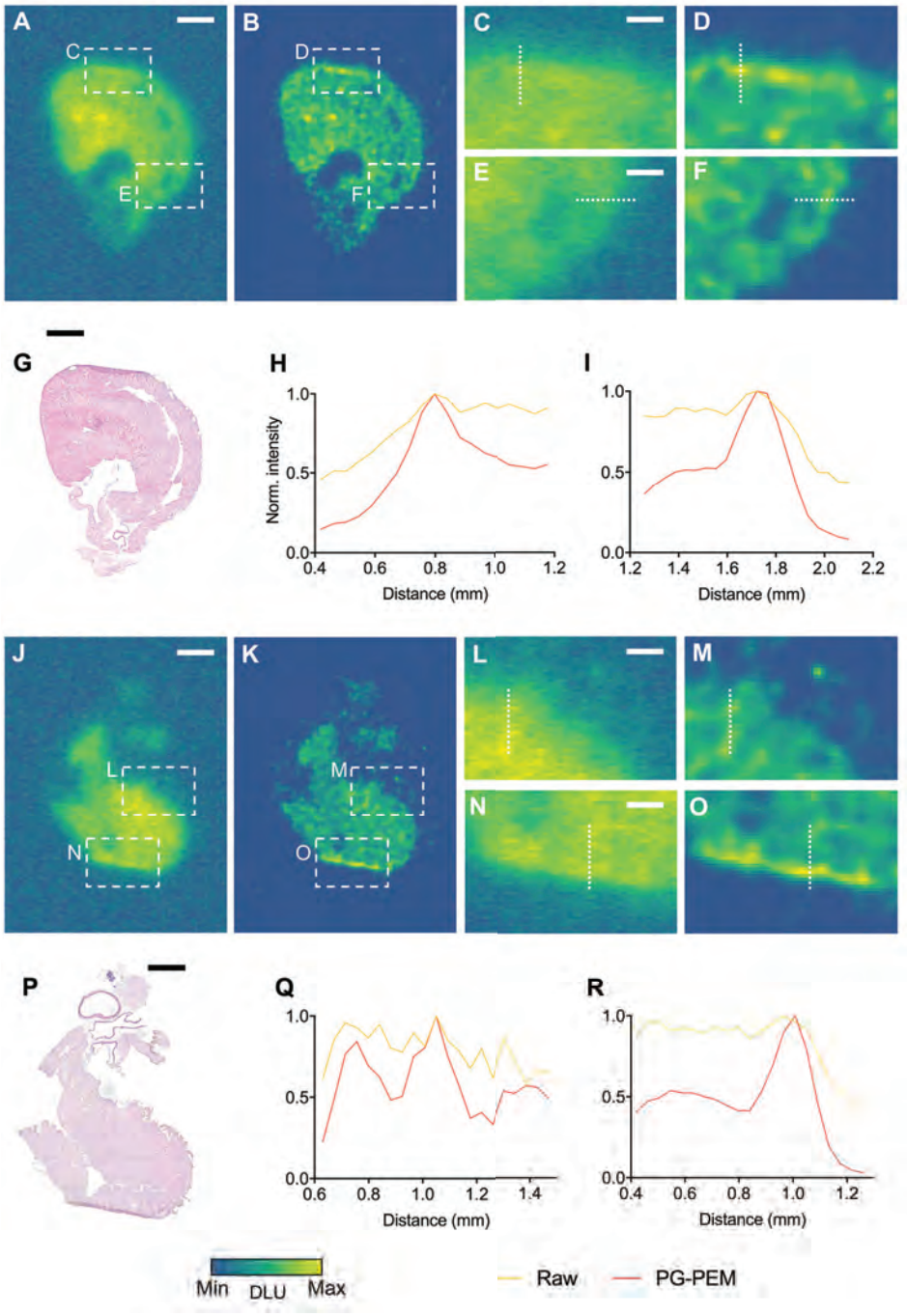

Supplementary Figure 15. PG-PEM improves the DAR image quality from [^{18}F]FDG administered murine heart. **(A,J)** Raw DAR images of mice heart sections. **(B,K)** Corresponding restored images of **(A,J)**. **(C–F)** Zoomed-in regions of the four dashed boxes in **(A,B)**. **(L–O)** Magnified Regions of Dashed Box Regions in **(J,K)**. **(G,P)** H&E stained tissue images corresponding to **(A,J)**. **(H,I,Q and R)** Line profile comparison along the corresponding dashed lines in **(C,E,L and N)**. Scale bar: **(A)**: 2.4 mm. **(C,E)**: 0.75 mm. **(G)**: 1.2 mm. **(J)**: 2.7 mm. **(L,N)**: 0.84 mm. **(P)**: 1 mm.

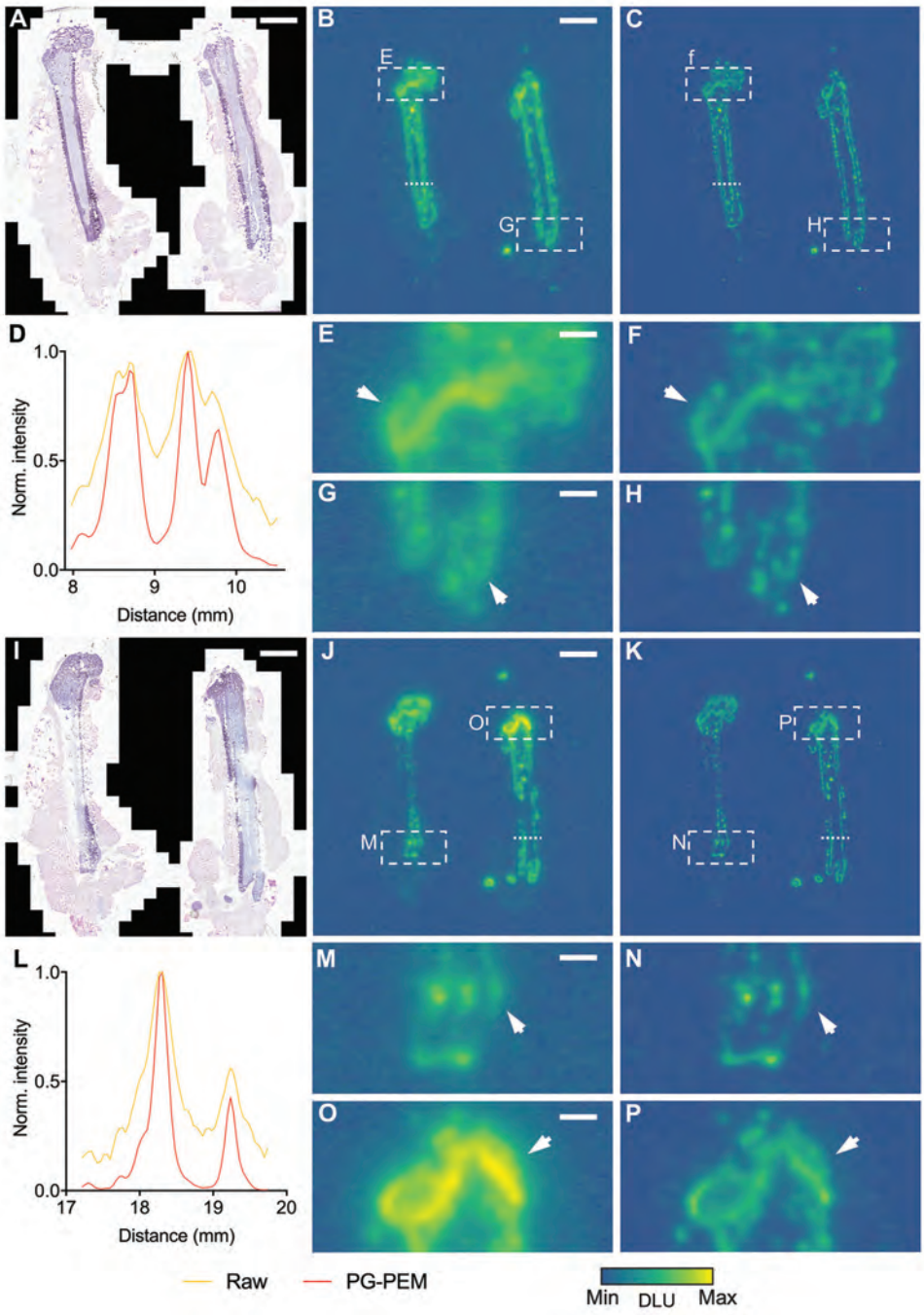

Supplementary Figure 16. PG-PEM improves DAR image quality from [^{18}F]NaF administered mouse femurs. **(A,I)** H&E stained mice femur images. **(B,J)** Corresponding raw DAR images of **(A,I)**. **(C,K)** The restored DAR images of **(B,J)** by PG-PEM. **(D,L)** Line profile comparison along the corresponding dashed lines in **(B,J)**. **(E–H)** Zoomed-in regions of the four dashed boxes in **(B,C)**. **(M–P)** Zoomed-in regions of the four dashed boxes in **(J,K)**. Scale bar: **(A)**: 2.25 mm. **(B)**: 3.15 mm. **(E,G)**: 0.67 mm. **(I)**: 2.3 mm. **(J)**: 3.2 mm. **(M,O)**: 0.68 mm.

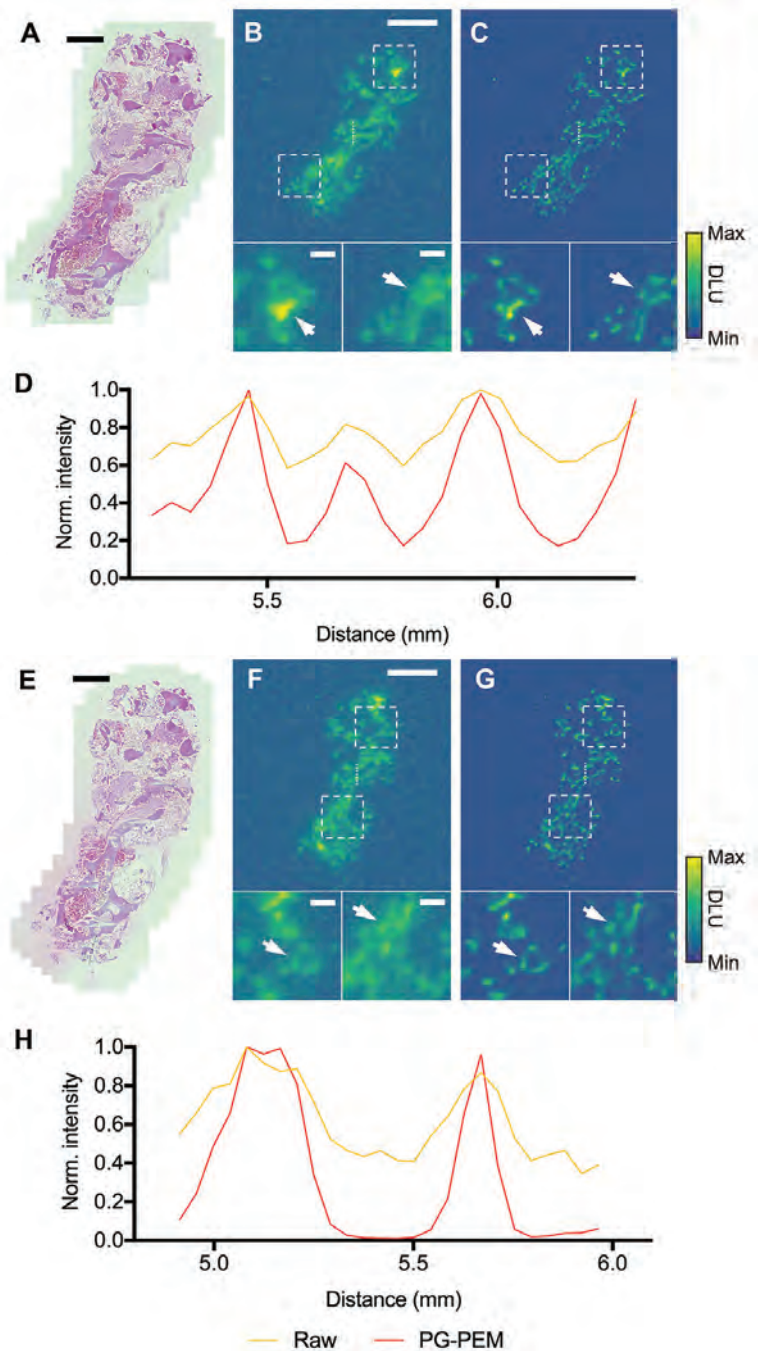

Supplementary Figure 17. PG-PEM improves DAR images of alpha particle radiotherapy. **(A,E)** H&E stained histopathological images of two human bone biopsy sections. **(B,F)** Corresponding Raw DAR images of the same section in **(A,E)**. **(C,G)** PG-PEM restored images of **(B,F)**. In **(B,C,F,G)**, the lower two images are the zoomed-in regions of the two dashed boxes in the upper images. **(D,H)** Line profiles in **(B,C,F,G)** along the corresponding dashed lines. Scale bar: **(A)**: 1 mm. **(E)**: 1.1 mm. **(B,F)**: first row: 2.3 mm, second row: 0.44 mm.

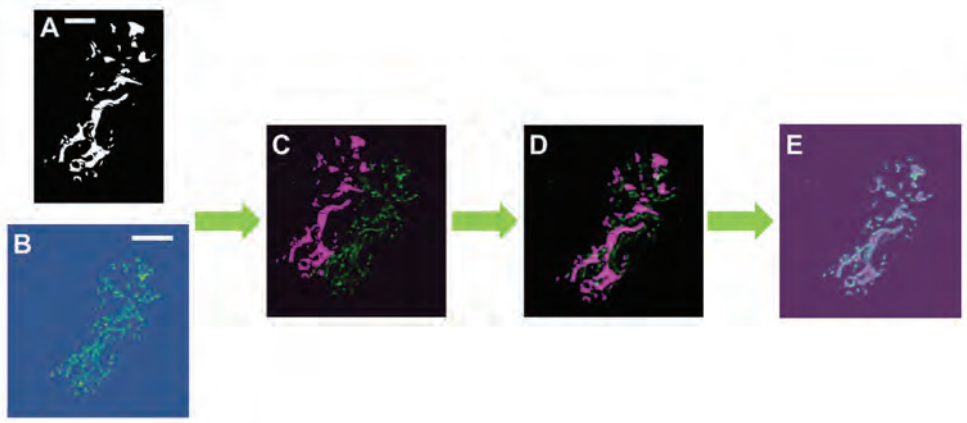

Supplementary Figure 18. Image resgistration process. **(A)** The segmented bone mask from a H&E stained histopathological image. **(B)** The corresponding PG-PEM restored DAR image. **(C)** Fused image before registration. **(D)** Initial registration: the bounding boxes of the two images are first found. Then the centers, areas and angles of the two boxes can be estimated. Next, the initial registration can be achieved by registering these two boxes including scaling, rotation and translation. **(E)** Final registration: maximize the mutual information between the two modalities by scaling, rotation and translation. Because the final registration algorithm is very easy to converge to a local minimum, the initial registration is essential. In our registration, we made the DAR image the fixed image and the bone mask the moving one. This is reasonable because 1) the pixel number of the bone mask is much bigger than that of the DAR image, and 2) the activity of the DAR image will be re-sampled and not the same as the original distribution if it is the moving image. Scale bar: **(A)**: 1 mm. **(B)**: 2.3 mm.

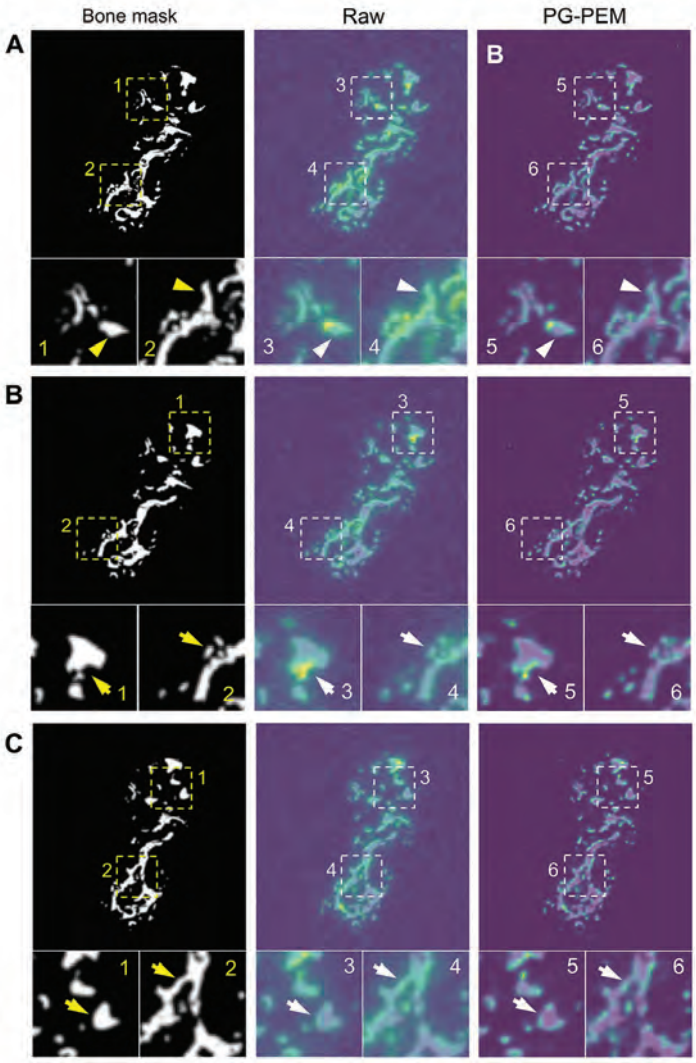

Supplementary Figure 19. Manually segmented bone mask, co-registered images of bone mask and DAR before and after restored by PG-PEM. (A) Figure 6. (B) Supplementary Fig 17(A)–(C). (C) Supplementary Fig 17(E)–(G).

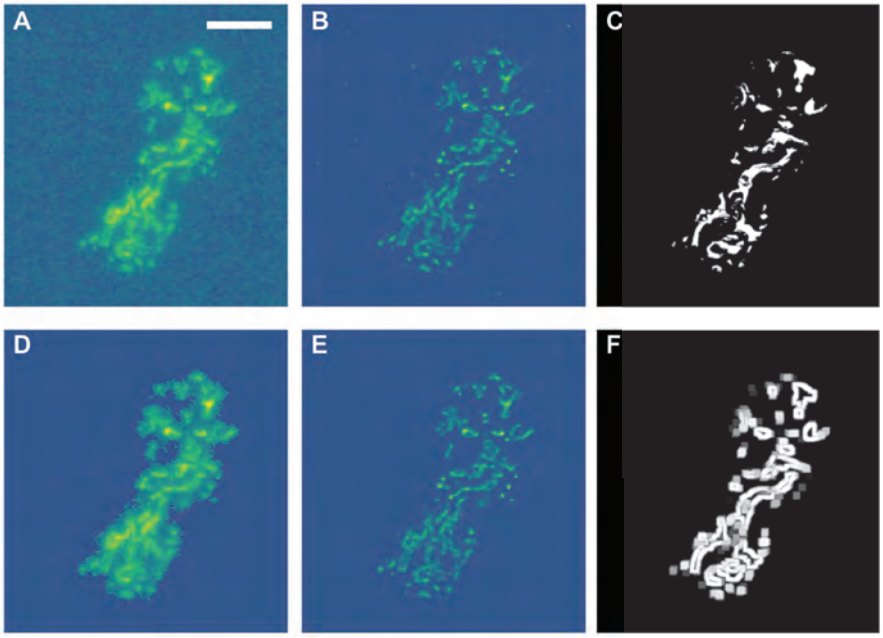

Supplementary Figure 20. SSIM and Fusion index estimation. **(A)** A raw DAR image of the human bone biopsy section. **(B)** The corresponding PG-PEM restored image. **(C)** The segmented bone mask from the corresponding H&E stained histopathological image. **(D)** High activity region of **(A)**. **(E)** High activity region of **(B)**. The estimation of the high activity region is achieved by a simple threshold method followed by removing small region. **(F)** The estimated bone surface from **(C)** using morphological operations: The bone mask is dilated and eroded by a small disk separately. Then the bone surface is estimated by subtracting the two results. We compare **(A)**, **(B)** with **(F)** to compute Fusion index and **(D)**, **(E)** with **(C)** to compute SSIM. Scale bar: **(A)**: 2.3 mm.

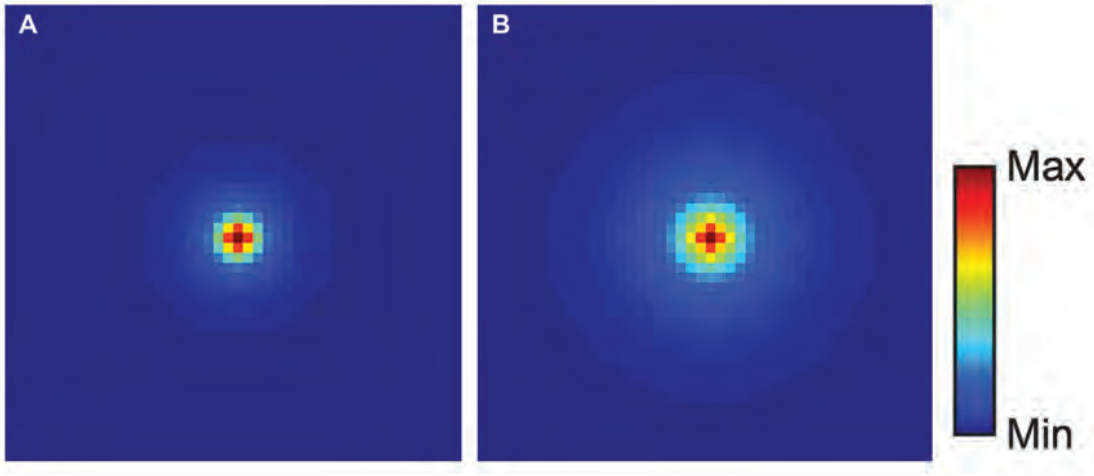

Supplementary Figure 21. PSF comparison. **(A)** The estimated PSF from a $^{223}RaCl_2$ treated human bone biopsy image. **(B)** The estimated PSF from a ^{18}F-NaF treated mouse hindlimb image. To increase the image contrast, we have applied a false coloured "jet" colormap. The estimated full-width half-maximum and full-width tenth-maximum of **(A)** are approximately 0.159 mm and 0.344 mm, while those of **(B)** are 0.216 mm and 0.66 mm, respectively. These results are consistent with the physics of alpha/positron transport: alpha particles have a significantly shorter path length than positrons. This is also why the raw autoradiographic images from ^{223}Ra treated human bone biopsy have higher resolution than those from ^{18}F treated sections. It should be noted that while several beta particles are produced by its daughters, the vast majority of the ^{223}Ra decay energy is in the form of alpha particles.

References

1. Janesick JR. Photon transfer noise sources. In: *Photon transfer DN→ λ.* Bellingham, Wash: SPIE Press; 2007: 21–25.

2. Mandracchia B, Hua X, Guo C, Son J, Urner T, Jia S. Fast and accurate sCMOS noise correction for fluorescence microscopy. *Nat Commun.* 2020;11:94.

3. Ester M, Kriegel HP, Sander J, Xu X. A density-based algorithm for discovering clusters in large spatial databases with noise. In: *KDD.* AAAI; 1996:226–231.

4. Crain BR. Estimating the parameters of a truncated normal distribution. *Appl Math Comput.* 1979;5:149–156.

5. Chouzenoux E, Jezierska A, Pesquet JC, Talbot H. A convex approach for image restoration with exact Poisson-Gaussian likelihood. *SIAM J Imaging Sci.* 2015;8:2662–2682.

6. Fish D, Brinicombe A, Pike E, Walker J. Blind deconvolution by means of the Richardson-Lucy algorithm. *J Opt Soc Am A Opt Image Sci Vis.* 1995;12:58–65.

7. Kenig T, Kam Z, Feuer A. Blind image deconvolution using machine learning for three-dimensional microscopy. *IEEE Trans Pattern Anal Mach Intell.* 2010;32:2191–2204.

8. Keuper M, Schmidt T, Temerinac-Ott M, *et al.* Blind deconvolution of widefield fluorescence microscopic data by regularization of the optical transfer function (OTF). In: *Proc IEEE Comput Soc Conf Comput Vis Pattern Recognit.* IEEE; 2013:2179–2186.

9. Koho S, Tortarolo G, Castello M, Deguchi T, Diaspro A, Vicidomini G. Fourier ring correlation simplifies image restoration in fluorescence microscopy. *Nat Commun.* 2019;10:3103.

10. Lefkimmiatis S, Bourquard A, Unser M. Hessian-based norm regularization for image restoration with biomedical applications. *IEEE Trans Image Process.* 2011;21:983–995.

11. Huang X, Fan J, Li L, *et al.* Fast, long-term, super-resolution imaging with Hessian structured illumination microscopy. *Nat Biotechnol.* 2018;36:451–459.

12. Ikoma H, Broxton M, Kudo T, Wetzstein G. A convex 3D deconvolution algorithm for low photon count fluorescence imaging. *Sci Rep.* 2018;8:11489.

13. Brune C, Sawatzky A, Burger M. Bregman-EM-TV methods with application to optical nanoscopy. In: *SSVM.* Elsevier; 2009:235–246.

14. Resmerita E, Anderssen RS. Joint additive Kullback-Leibler residual minimization and regularization for linear inverse problems. *Math Models Methods Appl Sci.* 2007;30:1527–1544.

15. Brownson JR. Chapter 03-Laws of light. In: *Solar Energy Conversion Systems.* Boston: Academic Press; 2014: 41–66.

16. Wang Z, Bovik AC, Sheikh HR, Simoncelli EP. Image quality assessment: from error visibility to structural similarity. *IEEE Trans Image Process.* 2004;13:600–612.

17. Descloux AC, Grussmayer KS, Radenovic A. Parameter-free image resolution estimation based on decorrelation analysis. *Nat Methods.* 2019;16:918–924.

18. Boussion N, Le Rest CC, Hatt M, Visvikis D. Incorporation of wavelet-based denoising in iterative deconvolution for partial volume correction in whole-body PET imaging. *Eur J Nucl Med Mol Imaging.* 2009;36:1064–1075.